On the Buckling Finite Element Analysis of Beam Structures

by

Denise Lori-Eng Poy

B.S., Mechanical Engineering (2000)
University of California, Berkeley

Submitted to the Department of Mechanical Engineering
in partial fulfillment of the requirements for the degree of

Master of Science in Mechanical Engineering

at the

MASSACHUSETTS INSTITUTE OF TECHNOLOGY

February 2002

Author ....
Department of Mechanical Engineering
January 17, 2002

Certified by...... ....
Klaus-Jürgen Bathe
Professor of Mechanical Engineering
Thesis Supervisor

Accepted by.................. ....
Ain A. Sonin
Chairman, Department Committee on Graduate Students

On the Buckling Finite Element Analysis of Beam Structures

by

Denise Lori-Eng Poy

Submitted to the Department of Mechanical Engineering
on January 17, 2002, in partial fulfillment of the
requirements for the degree of
Master of Science in Mechanical Engineering

Abstract

Large displacements and rotations are commonly encountered in the behavior of one-dimensional slender structures. There are several ways to model these structures using the finite element method, but since this involves a geometrically nonlinear analysis, a solution can be quite costly. By applying various assumptions developed from beam bending theory, the analysis can be considerably simplified. Further, the buckling analysis can be simplified to a linearized form for which there are two different formulations. In this thesis, the governing assumptions supporting the secant and classical methods for a linearized buckling analysis are compared.

This work surveys the effectiveness of various assumptions used in the analysis of one-dimensional slender structures, determines when they can be applied and examines their effects on bending and buckling behavior. By understanding when to appropriately apply the assumptions, we can characterize and model complex beam structures more effectively.

Three cases are modelled and evaluated to compare various assumptions. To gain further insight into the analyses, the solution techniques have also been implemented in a code developed specifically for evaluating the behavior of beam structures using a geometrically nonlinear finite element method.

Thesis Supervisor: Klaus-Jürgen Bathe
Title: Professor of Mechanical Engineering

Acknowledgments

First of all, I would like to express my sincere gratitude towards my advisor, Professor Klaus-Jürgen Bathe, for his patience and guidance. His tireless dedication to his students is truly admirable. I would also like to thank Jian Dong and the staff of ADINA R&D, Inc., for their assistance with this work.

My thanks also extend to my fellow graduate students at the Finite Element Research Group at MIT, Jung-Wuk Hong, Jean-François Hiller and Phill-Seung Lee. Thank you for showing me the ropes.

To the friends I have made at UC-Berkeley and MIT: I could not have endured these years without you, and I am grateful. Most of all, I would like to thank my mother Kit, my father George and my brothers Stephen and Matthew who never cease to amaze me with their unwavering confidence in my abilities and boundless wisdom and understanding.

Contents

List of Figures

List of Tables

Chapter 1

Introduction

Slender one-dimensional structures are often susceptible to large displacements and large rotations which complicate an analysis. These structures can be modelled as beams. The strains can be assumed to be small so that linearized constitutive equations can be applied, but the displacements and rotations are of arbitrary magnitude. For geometrically nonlinear systems undergoing this type of motion, the displacements are relatively large compared to the geometry of the problem. The kinematic relations are nonlinear resulting into that the element stiffness is a function of these displacements.

For geometrically linear behavior, the nonlinear terms are neglected, and this leads to a computationally less expensive linear analysis. However when including nonlinear behavior, the total displacement field must be computed incrementally as a continuous change in shape. At successive increments while the structure deforms, the analysis determines the solution with respect to the original undeformed configuration using the total Lagrangian description.

The displacement-based finite element method takes advantage of displacement interpolation functions to evaluate structures as models discretized into sufficiently small elements. The displacement functions and the finite element equations of equilibrium, which are based upon the principle of virtual work, can be used to solve for the displacement field of the body. This displacement field is continuous and satisfies the appropriate boundary conditions. Given the displacements and hence the strains, the stress-strain law is applied to obtain the internal nodal point forces which equilibrate the external forces. The geometrically nonlinear analysis described in this thesis was developed using the total Lagrangian formulation given in the article by K.J. Bathe and S. Bolourchi [4] and is adequate for large displacements and large rotations.

Frequently, in geometrically nonlinear analysis, in addition to determining the displacement field, one wants to determine the critical load a structure can withstand prior to instability. Structures undergoing large displacements and rotations are often unstable and can buckle under critical loads. This condition frequently occurs with slender structures under compressive loads. Instead of performing a computationally-expensive, complete incremental nonlinear analysis, a linearized buckling analysis can be employed to calculate the lowest buckling loads. This study will examine the ways to effectively model a beam structure which may be susceptible to instability.

An important aspect in successfully using the finite element method is to make the appropriate assumptions to decrease costs and the time consumed for a sufficiently effective analysis. There are many ways to effectively model structures and their behavior. The following study concentrates on beam models, a common type of finite element model found in many engineering applications. This study will also examine some of the different ways in which to simplify the finite element model and solution of a beam structure.

Much work has been done in this field of study, particularly for prismatic beam structures, but there are still many areas which need to be more carefully explored. The buckling instability of beam structures is a fundamental area of importance, and a thorough understanding of beam buckling behavior is necessary for the treatment of slender beam structures which are susceptible to collapse.

For simple cases, the beam behaviors under applied loading (e.g. displacement history and buckling loads) have been determined analytically. Most often, analytical results are not available for comparison with the finite element models of real-life applications. The finite element programs must be used with a clear understanding of the theoretical background to achieve reliable results. Two of the case studies examined in Chapter 3 compare the finite element results with analytical results, and the third case deals with a more complicated structure.

A general reference for the theoretical background and applications of the finite element method is provided by References [1] and [3]. A general derivation of the finite element method, including the secant formulation of linearized buckling analysis is given in Reference [3]. The formulation of the large displacement finite element analysis specifically using Hermitian beam elements is found in Reference [4].

General elastic beam bending theory using the Bernoulli beam assumption is studied in References [8] and [13], whereas the beam bending theory using the Timoshenko beam assumption can be found in Reference [16]. Stability and general beam buckling theory is discussed in References [7] and [15]. When applied to matrix methods, linearized buckling analysis using the classical formulation and general matrix iterative methods are developed in greater detail in References [6], [9] and [14].

The examples studied in Chapter 3 have been studied in other publications. Cases 1 and 2, common examples for studying large displacement bending and elastic instability respectively, can be found in papers such as [4] and [12]. Case 3 is introduced in Reference [2].

These studies show that errors develop when using Hermitian beam elements in the presence of moderate strains and significant shear forces. On the other hand, the isobeam elements gave accurate and reliable results with negligible variation when decreasing the number of nodes from four to two.

When performing a linearized buckling analysis, the accuracy of the secant formulation is reliant on the size of the perturbation load and converges in the limit as the perturbation load vanishes. On the other hand, the classical formulation is accurate and reliable, independent of the size of the perturbation load.

The equations were also implemented into a MATLAB code as discussed in Appendix B for the geometrically nonlinear finite element analysis of linear elastic beam structures using Hermitian beam elements. Implementation of the equations aids in understanding the solution process of the finite element method.

Chapter 2

Theory

To understand the behavior of beam structures, this work analyzes beams of rectangular section undergoing large deformations and rotations. When the analysis is no longer restricted to small displacements and rotations, the analysis can be adapted to model more complex behavior such as buckling.

The following approach uses an incremental total Lagrangian formulation in which the motion of the body is referenced to a fixed Cartesian coordinate system. The unknown static and kinematic variables in the configuration at time t are determined using those of the initial configuration. To determine these variables, the equations based on equilibrium, kinematics and constitutive behavior must be solved as described in the article by K.J. Bathe and S. Bolourchi [4]. A summary of the necessary equations used in this type of analysis is given in the following sections.

2.1 Beam Elements

The displacement-based finite beam elements used in the beam structure models are assumed to have constant cross-sectional area and remain straight due to the assumption of small strains. Hence, plane sections of the beam remain plane during deformation. Beam structures are most often modeled as assemblages of either two-node Hermitian or two-, three- or four-node isobeam elements. The main difference between the two major classes of beam elements, Hermitian and isobeam elements, lies in the assumptions used to model bending actions. The beam elements used to model the beam structures have six degrees of freedom per node and are capable of transmitting an axial force, two shear forces, a torque and two bending moments.

2.1.1 Hermitian Beam Elements

Hermitian elements exclude effects due to shear deformations and exhibit bending behavior corresponding with Bernoulli-Euler beam theory [8, 13]. The basic kinematic assumption governing Bernoulli-Euler beam theory for symmetric beams is that plane sections originally normal to the neutral axis remain plane after bending. In addition, the angular rotation is equal to the slope of the beam's mid-surface. The angle of the plane section measured from the vertical can be found using the relation [3]

$$\beta = \frac{dv}{dx} \tag{2.1}$$

where $v(x)$ is the transverse displacement along the beam originally lying along the x-axis and $\frac{dv}{dx}$ is the angular rotation of the element.

In the case of pure bending, the beam is subjected to a constant bending moment and therefore, the shear and axial forces are zero. Hermitian beam elements are ideal for the case of pure bending. For nonuniform bending, a shear force also acts on the beam, and the beam will shear and develop out-of-plane distortions. The absence of terms to account for shear deformations using Hermitian beams can yield questionable results. To account for the effect of shear forces, isobeam elements should be used.

2.1.2 Isobeam Elements

Isobeam beam elements include effects due to shear deformation and behave consistent with Timoshenko beam theory [16]. Timoshenko beam theory retains the assumption that plane sections through a beam remain plane after bending, but unlike the Bernoulli-Euler beam assumption, plane sections do not necessarily remain normal to the beam mid-section. Instead, these elements attempt to approximate the effects due to shear forces by assuming that the rotation of the plane section depends on a constant shearing strain across the section in addition to the rotation of the element. In other words, the angle of the plane section measured from the vertical β can be determined by the relation [3]

$$\beta = \frac{dv}{dx} - \gamma \tag{2.2}$$

where

$$\begin{aligned} \gamma &= \frac{\tau}{G} &&= \text{constant shearing strain over the corresponding shear area } A_s \\ \tau &= \frac{V}{A_s} &&= \text{shearing stress (shear force over the section } A_s\text{)} \\ k &= \frac{A_s}{A} &&= \text{shear correction factor determined from theoretical considerations [3]} \end{aligned}$$

Using the correction factor, the effects due to shear are closely approximated. A detailed analysis will be given in Chapter 3. The analysis will also compare the results using various multi-nodal elements.

The beam structure model can now be analyzed using the displacement-based finite element method. The basis for this method is the principle of virtual work from which we can extract and subsequently solve the equations of equilibrium.

2.2 Equations of Incremental Equilibrium

For linear analysis, the exact response corresponding to beam theory can be calculated because the exact displacement functions are known. These same functions are also used to yield an effective solution in nonlinear analysis, but whereas the stress-strain and compatibility relations are satisfied exactly, the stress equilibrium within the elements themselves is only satisfied approximately in the general case.

For example, consider a cantilever beam subjected to a transverse applied load at the tip. The results have been determined analytically and by using the finite element method by modelling the beam using ten Hermitian beam elements. The results are summarized in Appendix A. The stresses are calculated directly from the strains by applying the stress-strain law:

$$ {}_0^tS_{ij} = {}_0^tC_{ijrs}\, {}_0^t\epsilon_{rs} \tag{2.3} $$

These strains are evaluated from the displacements which are continuous and comply with the given displacement boundary conditions, thereby complying with compatibility. As shown in Figure A-3, the complex displacement field can be accurately represented using the finite element analysis compared to analytical theory. The accuracy of the finite element results for the displacements along the beam follows from the fact that the stress-strain law and compatibility are satisfied exactly. However, whereas the stress-strain law and compatibility are satisfied, the stress equilibrium is only satisfied approximately. Figure A-4 compares the analytical results to results from a finite element analysis for calculating the axial forces, shear forces and moments along the beam. Since the model is divided into a sufficient number of elements, the errors are minimal. When using a coarser mesh, the results start to skew as shown in Figure A-5 for a mesh using three elements. These findings agree with the statement that the finite element analysis satisfies stress equilibrium only approximately, whereas the stress-strain law and compatibility requirements are satisfied exactly.

Most geometric nonlinear analyses have been developed using three different formulations: total Lagrangian, updated Lagrangian and co-rotational. The total Lagrangian formulation utilizes the initial configuration as the reference frame (x_0, y_0, z_0 at time 0) described using the second Piola-Kirchoff stress and the Green-Lagrange strain. As suggested by its title, the updated Lagrangian formulation references the latest calculated configuration (x_t, y_t, z_t at time t) by using the same stress and strain measures but referred to time t to study the configuration at time $t + \Delta t$. The co-rotational formulation references a configuration that moves together with the element and allows the use of linear kinematic relations while the geometric nonlinearity is accounted for by the frame rotation.

In the total Lagrangian formulation, the principle of virtual work yields the following equation [4]:

$$({}^t_0\overline{K}_L + {}^t_0\overline{K}_{NL})\,\overline{u} = {}^{t+\Delta t}\overline{R} - {}^t_0\overline{F} \tag{2.4}$$

where

${}^t_0\overline{K}_L, {}^t_0\overline{K}_{NL}$ = linear and nonlinear incremental stiffness matrices

${}_0\overline{u}$ = vector of incremental nodal displacements

${}^{t+\Delta t}\overline{R}$ = vector of externally applied nodal loads at time $t + \Delta t$

${}^t_0\overline{F}$ = vector of nodal forces corresponding to element stresses at time t.

The subscript 0 preceding a quantity corresponds to a quantity measured in the total Lagrangian formulation with respect to the initial configuration at time 0. The overbar signifies a quantity evaluated with respect to the local convected coordinate axis of the beam ${}^t\overline{x}_i (i = 1, 2, 3)$. The finite element matrices listed above are evaluated using the following equations:

$$\begin{aligned} {}^t_0\overline{K}_L \, {}_0\overline{u} &= \left[\int_V {}^t_0\overline{B}_L^T \, {}_0\overline{C} \, {}^t_0\overline{B}_L \, dv\right] {}_0\overline{u} && (2.5) \\ {}^t_0\overline{K}_{NL} \, {}_0\overline{u} &= \left[\int_V {}^t_0\overline{B}_{NL}^T \, {}^t_0\overline{S} \, {}^t_0\overline{B}_{NL} \, dv\right] {}_0\overline{u} && (2.6) \\ {}^t_0\overline{F} &= \int_V {}^t_0\overline{B}_L^T \, {}^t_0\hat{S} \, dv && (2.7) \end{aligned}$$

where

${}^t_0\overline{B}_L, {}^t_0\overline{B}_{NL}$ = linear and nonlinear strain-displacement transformation matrices

${}_0\overline{C}$ = incremental stress-strain material property matrix

${}^t_0\overline{S}, {}^t_0\hat{S}$ = matrix and vector of second Piola-Kirchhoff stresses.

The linear and nonlinear strain-displacement transformation matrices are evaluated using the interpolation functions defined in Reference [4]. These functions are constructed assuming a linear variation in longitudinal, torsional and warping displacements and a cubic variation in transverse bending displacements.

The total Lagrangian formulation is characterized by the coordinate transformations required for the strain calculations. The transformation matrix ${}^{t}T$ relates the displacements measured in the original configuration at time 0 to the displacements measured in the current configuration at time t to account for the translational displacements and axial rotation of the beam elements. This transformation requires the additional equations:

$$\begin{aligned} {}^{t}_{0}K &= {}^{0}T^{T}_{0}\; {}^{t}\overline{K}\; {}^{0}T \qquad (2.8)\\ {}^{t}_{0}F &= {}^{0}T^{T}_{0}\; {}^{t}\overline{F} \qquad (2.9)\\ u &= {}^{0}T^{T}\; {}_{0}\overline{u} \qquad (2.10) \end{aligned}$$

where

${}^{t}_{0}K = {}^{t}_{0}K_L + {}^{t}_{0}K_{NL}$ = tangent stiffness matrix
${}^{0}T$ = transformation matrix
u = vector of incremental nodal displacements in the global coordinate system.

All quantities are explicitly defined in K.J. Bathe and S. Bolourchi [4] and are referred to the ${}^{0}\overline{x}_i (i = 1, 2, 3)$ coordinate system unless otherwise specified.

2.3 Incremental Analysis

An important feature of nonlinear analysis is incremental stepping. As the prescribed loads increase, the incremental displacement distributions are continuously calculated as incremental changes pertaining to each load step. The nonlinear stiffness matrix ${}^{t}_{0}K_{NL}$ also changes since it is dependent on the forces acting on the beam elements.

To appropriately calculate this nonlinear dependence, the final total load ${}^{t+\Delta t}\overline{R}$ must be divided into smaller increments, ${}^{\Delta t}\overline{R}$, and applied successively to the structure at each timestep Δt. Additionally at each step, the incremental displacements are calculated and added to the incremental displacements previously calculated over all previous timesteps as shown by the following equation:

$$^{t+\Delta t}U = {}^{t}U + U \tag{2.11}$$

where U is the increment in nodal displacements corresponding to the increment in element displacements and stresses from time t to time $t + \Delta t$. A similar incremental relationship holds for the nodal point force vector $^{t+\Delta t}F$. For problems with multiple loads, the incremental load vector can be implemented using different scaling factors for the various loads.

Usually the errors resulting from the first linearized calculation of the internal stresses are too large to be negligible. In this case, the Newton-Raphson iterative method is employed to maintain equilibrium between the applied loads and the internal stresses.

2.4 Newton-Raphson Iterations

The tangent stiffness matrix, $^{t+\Delta t}K^{(0)}$, is only an approximation since it was derived by linearization. After i iterations, the resulting matrix, $^{t+\Delta t}K^{(i)}$, is progressively a more accurate representation of the true linearized behavior at time $t + \Delta t$.

For each load step, equilibrium is attained when the external load vector equals the internal stress vector such that [3]

$$^{t+\Delta t}R - {}^{t+\Delta t}F = 0 \tag{2.12}$$

The external load vector, $^{t+\Delta t}R$, is simply a vector comprised of externally applied nodal loads and is independent of the displacements. The internal stress vector, $^{t+\Delta t}F$, must be calculated at each incremental step since it depends on the total displacements corresponding to that timestep. To correct the error in the incremental approach described in Section 2.3, the Newton-Raphson iterative scheme is included. This scheme assumes an initial value of $^{t+\Delta t}F = {}^{t}F$, corresponding to the internal stresses found at the previous timestep. As the load increases from ${}^{t}R$ to ${}^{t+\Delta t}R$, the internal stresses also increase. The Newton-Raphson iterations increase the magnitude of ${}^{t+\Delta t}F$ until it matches the known external nodal loads, ${}^{t+\Delta t}R$ at the timestep. The iterative error, the difference between the two vectors, is used to calculate the incremental displacements in the timestep. These incremental displacements decrease from the start of each timestep as the Newton-Raphson method converges and Equation 2.12 is satisfied to within an acceptable tolerance. The equations used in this process are summarized below for iteration $i = 1, 2, 3, \ldots$:

$$\begin{aligned} {}^{t+\Delta t}K^{(i-1)}\Delta U^{(i)} &= {}^{t+\Delta t}R - {}^{t+\Delta t}F^{(i-1)} && (2.13) \\ {}^{t+\Delta t}U^{(i)} &= {}^{t+\Delta t}U^{(i-1)} + \Delta U^{(i)} && (2.14) \end{aligned}$$

with the following initial conditions per step

$${}^{t+\Delta t}K^{(0)} = {}^{t}K; \qquad {}^{t+\Delta t}U^{(0)} = {}^{t}U; \qquad {}^{t+\Delta t}F^{(0)} = {}^{t}F$$

To derive Equations 2.13 and 2.14, we express the finite element equilibrium equations 2.12 as

$$f(U^*) = 0 \tag{2.15}$$

where

$$f(U^*) = {}^{t+\Delta t}R(U^*) - {}^{t+\Delta t}F(U^*) \tag{2.16}$$

and U^* represents the final solution vector of displacements. Taking a Taylor series expansion of $f(U^*)$ yields

$$f(U^*) = f({}^{t+\Delta t}U^{(i-1)}) + \left[\frac{\partial f}{\partial U}\right]\Bigg|_{{}^{t+\Delta t}U^{(i-1)}} (U^* - {}^{t+\Delta t}U^{(i-1)}) + \text{ higher-order terms} \tag{2.17}$$

given that the vector of displacements ${}^{t+\Delta t}U^{(i-1)}$ is evaluated at the previous iteration.

Substituting Equations 2.15 and 2.16 into Equation 2.17 and ignoring the higher-order terms results in

$$\left[\frac{\partial F}{\partial U}\right]\Bigg|_{{}^{t+\Delta t}U^{(i-1)}} (U^{*} - {}^{t+\Delta t}U^{(i-1)}) = {}^{t+\Delta t}R - {}^{t+\Delta t}F^{(i-1)} \tag{2.18}$$

assuming that the externally-applied loads are independent of the displacements, i.e. $\frac{\partial R}{\partial U} = 0$ and ${}^{t+\Delta t}R$ is constant throughout the timestep. This equation can be simplified to Equation 2.13 where

$${}^{t+\Delta t}K^{(i-1)} = \left[\frac{\partial F}{\partial U}\right]\Bigg|_{{}^{t+\Delta t}U^{(i-1)}} \tag{2.19}$$

The final displacement solution converges by improving the displacement solution using Equation 2.14. In practice, this process is repeated until the convergence is reached with sufficiently small $\Delta U^{(i)}$ or sufficiently small $({}^{t+\Delta t}R - {}^{t+\Delta t}F^{(i)})$.

2.5 Linearized Buckling Analysis

Structures undergoing large displacements and rotations are often unstable and can buckle or collapse. This condition particularly occurs to slender structures undergoing compressive loads. One way to determine the critical buckling load can be through evaluating the load displacement history as outlined in the previous section. The total stiffness matrix at any time τ, ${}^{\tau}_{0}K$, changes as the load increases with time. For loads smaller than the critical load, the internal and external forces acting on the beam are in stable equilibrium, and the deflections remain relatively small. In general, when the forces in the beam are mostly tensile, the total stiffness increases; when the forces are mostly compressive, the total stiffness decreases. When the stiffness decreases, the structure is susceptible to buckling. As the total stiffness approaches zero, the displacement increments increase rapidly until reaching a certain point at which the system is unstable. This limit point represents the point at which the internal and external forces are in unstable equilibrium. The value of the applied load has reached the critical buckling load value given by

$$ {}^{\tau}_{0}Ku = 0; u \neq 0 \tag{2.20} $$

with ${}^{\tau}_{0}K$ singular which leads to

$$ \det[{}^{\tau}_{0}K] = 0 \tag{2.21} $$

In most cases, this procedure is expensive. Often, the load increments specified are not small enough to correctly detect when Equation 2.21 is fulfilled, and calculating through each incremental load until buckling is costly. An automatic time-stepping approach such as the load-displacement-constraint (LDC) method can be used for a nonlinear displacement analysis that steps through each incremental load.

A more efficient alternative to calculating the lowest buckling loads is the linearized buckling analysis. Instead of calculating through each time step to find the displacement history, the linearized buckling analysis assumes that the elements of the stiffness matrix vary linearly from time $t - \Delta t$ until the time t when buckling occurs. The buckling load is approximated using sufficiently small prebuckling loads. The problem is effectively reduced to an eigenvalue problem with which we want to evaluate the eigenvalues and eigenvectors to find the corresponding buckling loads and mode shapes.

At the point of instability, the application of the critical buckling load, the stiffness matrix is singular. Therefore, Equation 2.20 can be rewritten as

$$ {}^{\tau}_{0}K\phi_i = 0 \tag{2.22} $$

where ϕ_i is a nonzero vector corresponding to buckling mode i. This analysis can be quite accurate if used with sufficiently small prebuckling displacements. For a detailed look into the calculation of the linearized buckling load, there are two formulations: the secant and classical formulations.

2.5.1 Secant Formulation

Linearized buckling analysis using the secant formulation assumes that the elements of the stiffness matrix vary linearly from the previous timestep to the time of buckling. This assumption likewise applies to the vector of external loads. Therefore, the following relations hold at any time τ [3]:

$$ {}^{\tau}_{0}K = {}^{t-\Delta t}_{0}K + \lambda_i \, ({}^{t}_{0}K - {}^{t-\Delta t}_{0}K) \tag{2.23}$$

and

$$ {}^{\tau}_{0}R = {}^{t-\Delta t}_{0}R + \lambda_i \, ({}^{t}_{0}R - {}^{t-\Delta t}_{0}R) \tag{2.24}$$

where λ_i is a scaling factor corresponding to buckling modes $i = 1, 2, 3, \ldots$ and the stiffness matrices and corresponding vectors of externally applied loads, ${}^{t-\Delta t}_{0}K$, ${}^{t}_{0}K$, ${}^{t-\Delta t}_{0}R$ and ${}^{t}_{0}R$, are known. By substituting Equation 2.23 into Equation 2.20, we obtain the generalized eigenvalue problem:

$$ {}^{t-\Delta t}_{0}K\phi_i = \lambda_i \, ({}^{t-\Delta t}_{0}K - {}^{t}_{0}K)\phi_i \tag{2.25}$$

The resulting λ_i and ϕ_i correspond to the critical buckling loads and buckling modes. Since ${}^{t-\Delta t}_{0}K - {}^{t}_{0}K$ is indefinite, this yields both positive and negative eigenvalues. To calculate the smallest positive eigenvalues, we rewrite Equation 2.25 as

$$ {}^{t}_{0}K\phi_i = \xi_i \, {}^{t-\Delta t}_{0}K\phi_i \tag{2.26}$$

where

$$ \xi_i = \frac{\lambda_i - 1}{\lambda_i} \tag{2.27}$$

The values of ξ_i are strictly positive. By using this transformation, the eigenvalues are strictly positive and the smallest one corresponds to the lowest buckling mode.

The buckling loads are evaluated from the eigenvalues using the following equation:

$$R_{buckling,i} = {}^{t-\Delta t}_{\;\;0}R + \lambda_i \left({}^{t}_{0}R - {}^{t-\Delta t}_{\;\;0}R\right) \tag{2.28}$$

2.5.2 Classical Formulation

Linearized buckling analysis using the classical formulation takes advantage of different assumptions to derive a solution to Equation 2.22. The classical formulation takes advantage of the fact that the tangent stiffness matrix can be broken down into a linear part and a nonlinear part as shown in Section 2.2 such that ${}^{\tau}_{0}K = ({}^{\tau}_{0}K_L + {}^{\tau}_{0}K_{NL})$. Substituting this relation into Equation 2.22 yields

$$\left({}^{\tau}_{0}K_L + {}^{\tau}_{0}K_{NL}\right)\phi_i = 0 \tag{2.29}$$

for any time τ. We assume that the total tangent stiffness matrix varies linearly in time during prebuckling; hence, the term, "linearized" buckling analysis. The linear part of the incremental stiffness matrix is assumed to be independent of loading and to remain constant as the loading increases with time. Therefore, the time-dependence of the total stiffness matrix originates from the nonlinear stiffness matrix which simply varies as a multiple of its initial value:

$${}^{\tau}_{0}K_L + {}^{\tau}_{0}K_{NL} \approx {}^{0}_{0}K_L + \lambda_i \, {}^{\Delta t}_{\;0}K_{NL} \tag{2.30}$$

If we generalize this statement such that the linear portion of the stiffness matrix is constant and equal at any time τ to the linear stiffness matrix at some time t, then substituting this approximation into Equation 2.29 leads to the following equation:

$$\left({}^{t}_{0}K_L + \lambda_i \, {}^{t}_{0}K_{NL}\right)\phi_i = 0 \tag{2.31}$$

since K_L is constant for all t. The buckling loads and corresponding buckling modes can then be found using the following equation [1]:

$$ {}_{0}^{t}K\phi_i = \xi_i\,({}_{0}^{t}K - {}_{0}^{t}K_{NL})\phi_i \tag{2.32} $$

where ξ_i is defined exactly as in Equation 2.27 for the secant formulation. The critical buckling loads are then calculated using Equation 2.28. The classical formulation is widely used and can be found in many texts on finite element methods.

2.6 Warping Torsion Analysis

Warping torsion occurs in prismatic beams of noncircular cross-section which are subject to twisting. In ADINA, the isobeam and Hermitian beam elements both model the warping behavior as derived in the paper by K.J. Bathe and A.B. Chaudhary [1, 5].

To implement a warping torsion analysis using beam elements, separate warping displacement functions must be included in the formulation of the beam element to account for the additional axial displacements that occur under large torques. St. Venant torsion theory of a non-circular twisted bar assumes that the deformation is comprised of two components. First, every cross-section along the bar rotates as a function of θ, the angle of twist per unit length of the bar [10]. Second, every cross-section warps by some amount u = $\psi(x,y)$ where $\psi(x,y)$ is a general warping function dependent on the shape of the cross-section. For beams of general rectangular cross-section [5]:

$$ u = \alpha xy + \beta xy(x^2 - y^2) \tag{2.33} $$

where α and β are additional degrees of freedom which may be eliminated using static condensation before assembling the global stiffness matrix. The displacements v and w are given by the general linear functions for torsion [3, 4]. There are no normal stresses acting between the longitudinal fibers, and this warping component acts identically over all cross-sections of the beam. The addition of these warping displacements will affect the linearized buckling analysis in addition to the total displacement field.

The analysis defined using the procedure outlined above can now be applied to the following examples for which we will compare the results of these two linearized buckling methods.

Chapter 3

ADINA Case Studies

Three cases were analyzed using the finite element analysis commercial software package ADINA. The finite element large displacement and linearized buckling analysis results were compared to analytical results, if available. The following cases are limited to isotropic, linear elastic material behavior for large displacements and rotations.

3.1 Cantilever Beam Subjected to End Moment

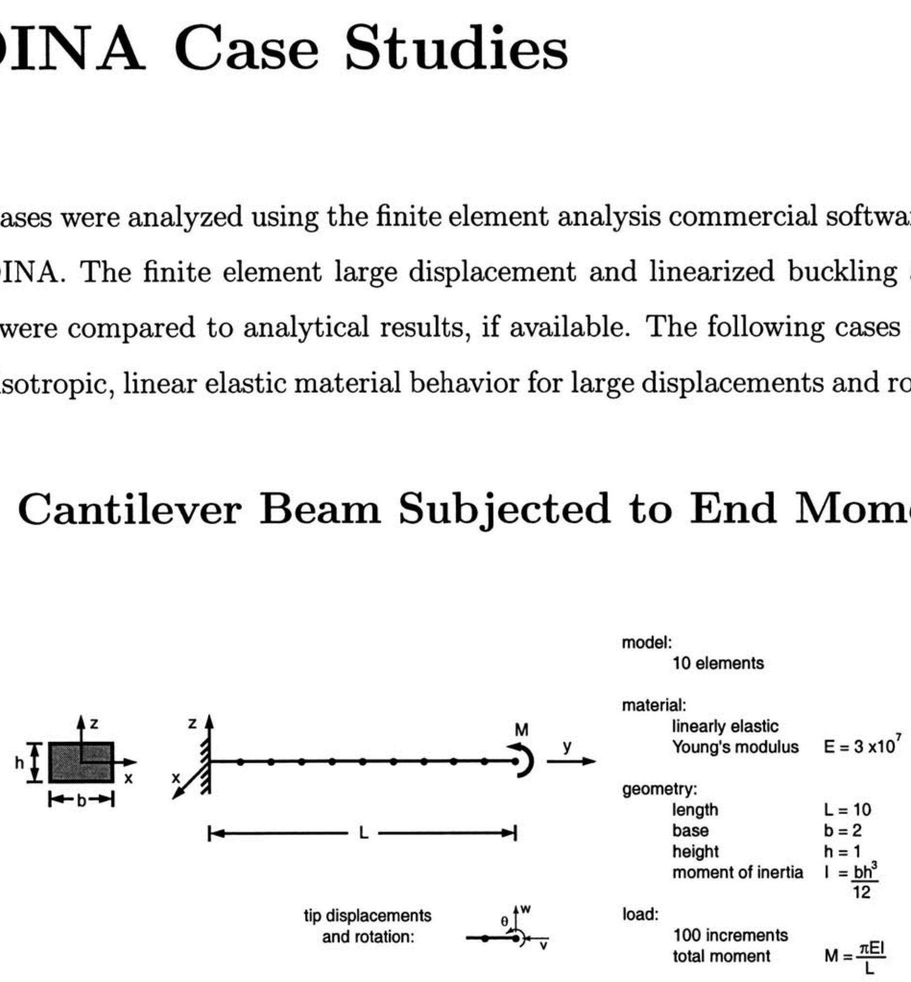

Figure 3-1: Cantilever beam under end moment: finite element model

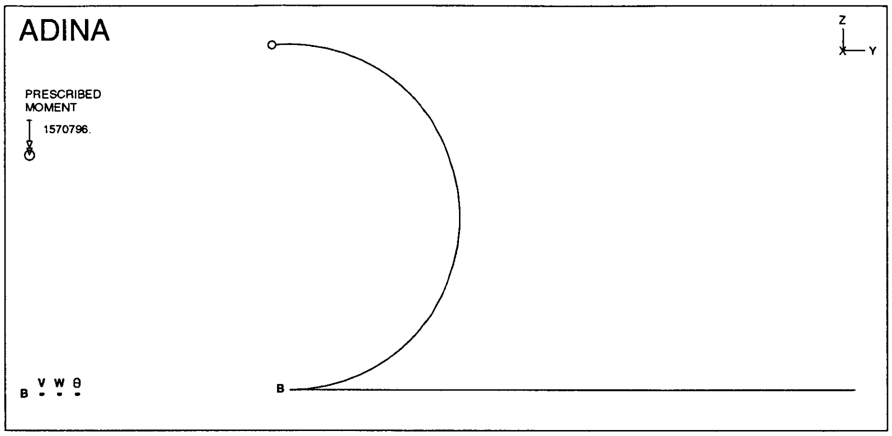

Figure 3-2: Case I: motion following the load application

The beam is initially straight and is idealized using ten elements with motion restricted to the y-z plane as shown in Figure 3-1. Figure 3-2 illustrates the resulting two-dimensional beam motion due to the concentrated end moment M. The two beam configurations correspond to the motion corresponding moment parameters $\eta = 0$ and $\eta = 0.9$, respectively. The following discussion will look at the limitations of the analytical solution compared to a more complete large deformation finite element analysis.

3.1.1 Analytical Solution Using Bernoulli Beam Assumption

Since there is only an applied moment acting on the end of the beam, the internal reaction consists of a constant bending moment along the length of the beam. This case is idealized in solid mechanics as one of pure bending, where the only resultant internal reaction is a pure couple. Therefore, there are no shear or axial forces, and there is no danger of instability in the analysis.

The theory behind pure bending states that the cross section is plane along the length of the beam and remains plane under bending. This assumption also corresponds with the fundamental Bernoulli beam assumption discussed in Section 2.1.1 for Hermitian beam elements. By applying this Bernoulli beam assumption to this particular case, we can easily derive equations to analytically calculate the nodal displacements and rotations. The Bernoulli beam assumption is applicable to beam structures undergoing large displacements, large rotations and small strains.

There is an infinitesimal angle $d\theta$ between two planes initially normal to the neutral axis when the beam is in bending. These two initially normal planes intersect the neutral axis at two distinct points which are separated by an infinitesimal distance ds along the curved beam. Therefore, the following geometric relation holds for a beam undergoing small strains such that $dy = ds$:

$$\frac{1}{\rho} = \frac{d\theta}{ds} \tag{3.1}$$

where ρ is the radius of curvature of the beam after bending. By applying Hooke's law and balancing linear momentum about the neutral axis, the exact differential equation for the deflection curve can be expressed as

$$EI\frac{d\theta}{ds} = M \tag{3.2}$$

for beams of Young's modulus E and moment of inertia I.

This equation can be recast as the general moment-curvature relationship applicable to beams of linearly elastic material:

$$\frac{1}{\rho} = \frac{M}{EI} \tag{3.3}$$

In order to achieve such a simple equation relating moment and curvature, we must assume that the strains and relative rotations are small and therefore, the incremental slope of the beam is very small. This small strain assumption leads to a slight error in the analysis which will be addressed in the following section.

By substituting the moment-curvature relation, Equation 3.3, into the simple geometrical relations derived in Figure 3-3, the displacements and rotations can be

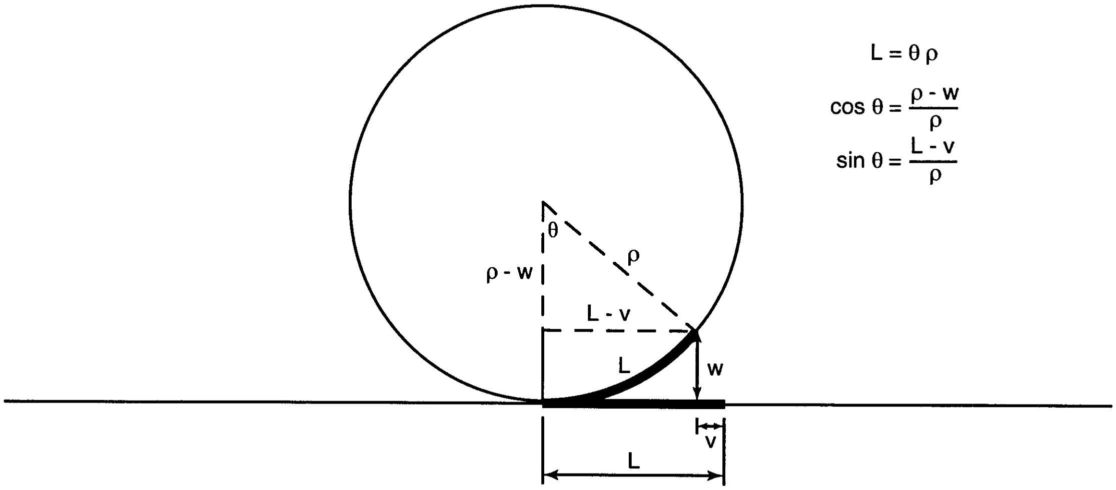

Figure 3-3: Case I: derivation of the analytical solution

found analytically from the given material and loading conditions:

$$\text{axial displacement, v} = L - \frac{EI}{M}\sin\left(\frac{ML}{EI}\right) \tag{3.4}$$

$$\text{transverse displacement, w} = \frac{EI}{M}\left[1 - \cos\left(\frac{ML}{EI}\right)\right] \tag{3.5}$$

$$\text{rotation, } \theta = \frac{ML}{EI} \tag{3.6}$$

By restricting the analysis to one of Bernoulli beam bending, the mathematics becomes much simpler and can be completed without running a more costly finite element analysis. The main consequence of this simplification is an error which will be evaluated and addressed in the following sections.

3.1.2 Finite Element Analysis

The normalized moment-displacement curve of Figure 3-4 compares the ADINA analyses using Hermitian and multi-nodal isobeam elements and the analytical results. The plot shows the normalized nodal y-displacements $\frac{v}{L}$, the normalized nodal z-displacements $\frac{w}{L}$ and the normalized nodal rotations $\frac{\theta}{2\pi}$ at the tip of the beam. The load-displacement results from analytical theory and the Hermitian beam analysis are

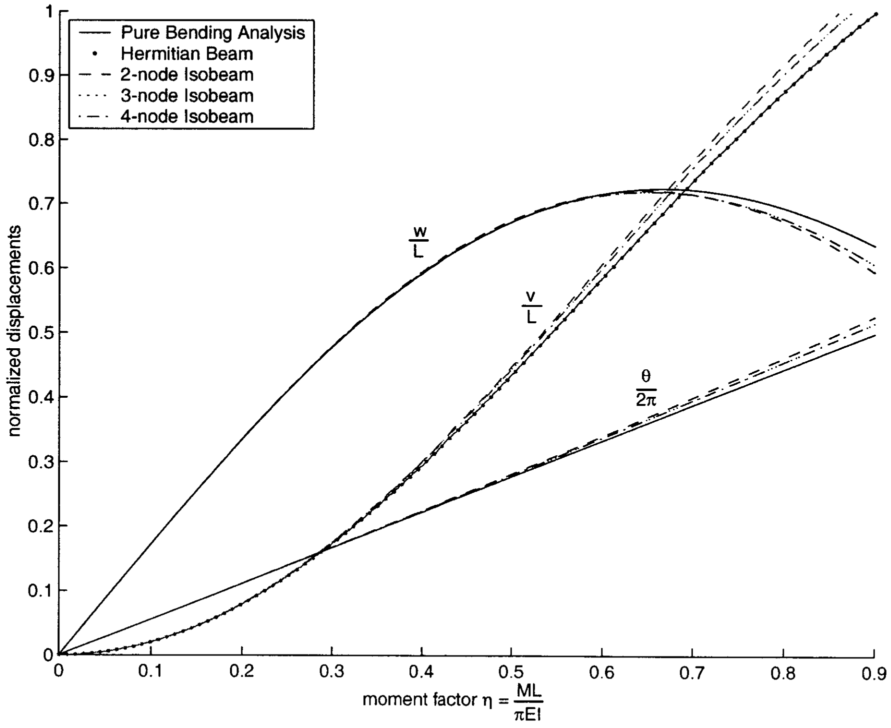

Figure 3-4: Case I: load-displacement plot of the tip for a thick beam; L = 10
Note: The results for the three-node and four-node isobeam element are overlapping.

Beam Element Type	$\frac{v}{L}$ y-displacements		$\frac{w}{L}$ z-displacements		$\frac{\theta}{2\pi}$ x-rotations	
	Value	Difference	Value	Difference	Value	Difference
Analytical	1.00000	3.016%	0.63662	4.919%	0.50000	3.157%
Hermitian beam	1.00000	3.016%	0.63924	5.352%	0.50000	3.157%
2-node isobeam	1.04937	1.741%	0.59514	1.954%	0.52634	1.908%
3-node isobeam	1.03112	0.002%	0.60676	0.002%	0.51631	0.002%
4-node isobeam	1.03110		0.60677		0.51630	

Table 3.1: Case I: convergence properties at the tip for a thick 10-element beam; L = 10

practically identical and differ within less than one percent.

There is a noticeable discrepancy between the Hermitian beam and analytical results and the isobeam results in Figure 3-4. Table 3.1 compares the values of the displacements at the tip of the beam for the various beam models. From the theory discussed in Section 2.1, one can assume that the four-node isobeam is the most accurate solution since it can be applied to more general large displacement and strain cases. Therefore, the error analysis for the other beam models was based on the four-node isobeam analysis. After performing additional tests on the isobeam element, it can be concluded that the discretization error is negligible for this case, and there is no evident source of error from the convergence tolerances for the shear analysis using the isobeam element.

The plot in Figure 3-4 shows that the isobeam transverse displacements are larger than those from the analytical theory and the Hermitian beams by as much as 5%. To find the cause of this error, one must return to the underlying assumptions used in the models of the Hermitian beam and isobeam elements. One notable difference between the two models is the less refined level of approximation for the strain-displacement relation for the Hermitian beam element. The Hermitian beam element and Bernoulli beam theory neglects a higher order strain term so that they are essentially valid for sufficiently small strains.

The 5% error for the analytical and Hermitian analyses arises primarily from this small strain assumption. As mentioned in its derivation, the analytical solution assumes small strains. Likewise, the derivation of the equations for the Hermitian beam element eliminates higher-order quadratic terms from the Green-Lagrange strain matrix, ${}_0^t\epsilon_{rs}$, in the total Lagrangian formulation equations given in Section 2.2. The Piola-Kirchoff stresses are found from the Green-Lagrange strains using the stress-strain law from Equation 2.3. The strain-displacement relation for the axial strain component of a three-dimensional bending beam lying along the y-axis is the following [3]:

$$\epsilon_{yy}^* = \frac{\partial v^*}{\partial y} + \frac{1}{2}\left[\left(\frac{\partial w^*}{\partial y}\right)^2 + \left(\frac{\partial v^*}{\partial y}\right)^2\right] \tag{3.7}$$

where v^* and w^* are the displacements of a longitudinal fiber along the beam in the y- and z-directions, respectively, and are functions of the transverse position of the fiber in the z-direction in addition to the axial and transverse displacements v and w (*i.e.* $v^* = f(v, w, z)$ and $w^* = g(v, w, z)$). The higher-order z-dependent terms are neglected for small strain analysis. These terms become more pronounced when the beam is thicker, and this causes an error in small strain analyses that use the Bernoulli beam assumption. Since the strains are larger in thicker beams, this small strain approximation causes the Hermitian beam element response to stray from the isobeam response when the beam thickness increases. Unlike the Hermitian beam element, the isobeam element is capable of effectively modelling larger strains.

Beam thickness is usually evaluated using the nondimensional slenderness ratio, $\frac{L}{d}$ where d is the depth of the beam in the plane of bending. For thicker beams, approximately $\frac{L}{d} < 10$, the additional terms in the strain expression are significant, and the errors in the analysis increase.

Figure 3-5 is a plot of the same beam when the length of the beam is increased by a factor of ten so that L = 100. Lengthening the beam, and thereby decreasing its thickness to length ratio results in the decrease of the magnitude of the strains. In the limit as the strains become very small, the beam becomes increasingly more slender and the isobeam results converge towards the Hermitian beam and analytical results.

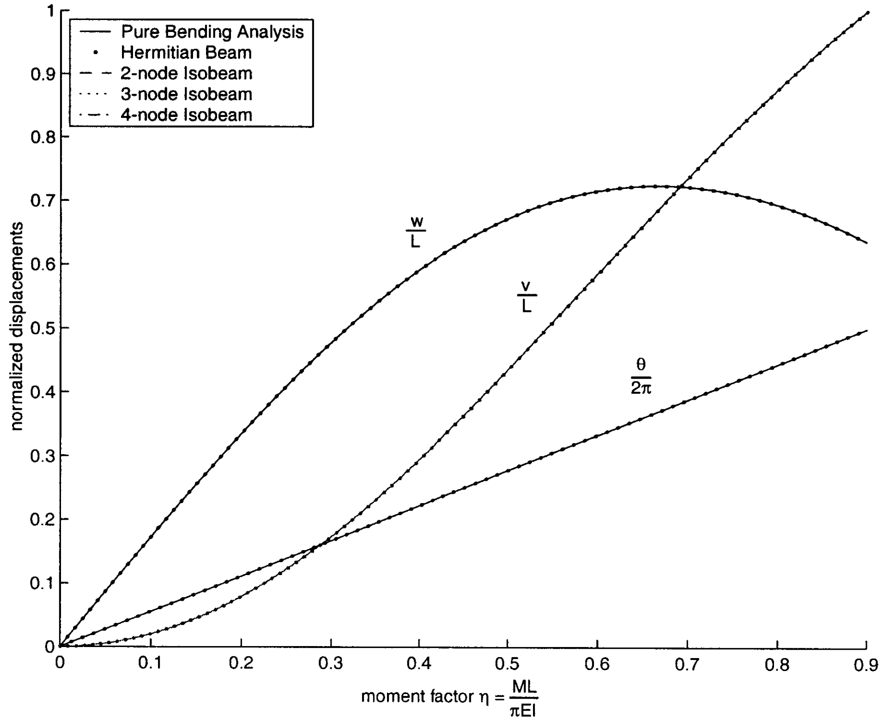

Figure 3-5: Case I: load-displacement plot of the tip for a slender beam; L = 100

Figure 3-5 shows that the results of the isobeam elements match the solution derived from the Bernoulli beam assumption when the beam length L = 100. The differences in the normalized tip deflections and rotations are less than one-thousandth. Therefore, it is usually only necessary to use the more numerically complex Timoshenko beam assumption in the analysis for thicker beams when the strains are larger. The evaluation of thick beam structures should be restricted to isobeam elements. For slender beams, the Hermitian beam elements are sufficient.

Figure 3-4 also illustrates the convergence properties of the isobeam element as the number of nodes increases. As the number of nodes per element increases from two to four, the results given in Table 3.1 converge rapidly. It should also be noted that the three-node element performs just as well as the four-node element for this analysis.

3.2 Cantilever Beam Subjected to Compressive Load

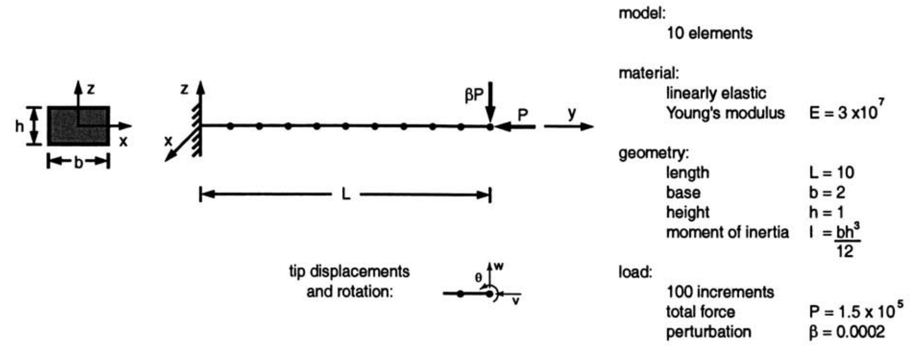

Figure 3-6: Cantilever beam under compressive axial load: finite element model

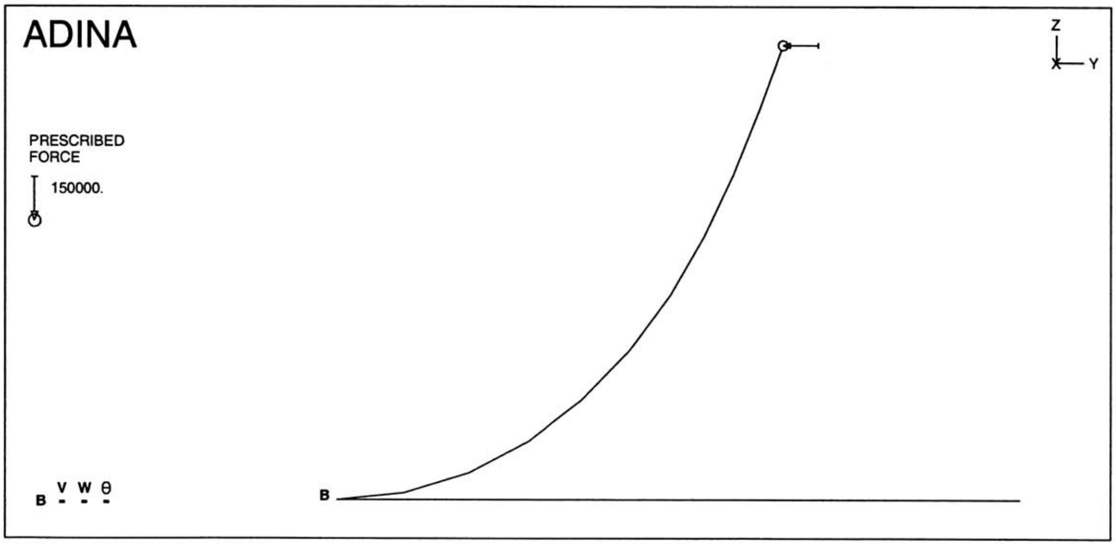

Figure 3-7: Case II: motion following load application

For this case, a cantilever beam modelled with ten beam elements is subjected to an axial compressive load P and a transverse perturbation load βP at the tip of the beam. The problem description is shown in Figure 3-6. Initially, the beam is straight and of constant rectangular cross section. The resulting beam motion is restricted to the y-z plane, and the deflected shape is illustrated in Figure 3-7 for $P = 1.5 \times 10^5$.

3.2.1 Analytical Solution Using Bernoulli Beam Assumption

One way to analyze this problem is similar to the previous analysis using the Bernoulli beam assumption. Shear deformations are ignored, and we will show that this is acceptable for slender bars. By obtaining an approximate solution to the deflection curve (similar in form to Equation 3.2 where the bending moment can be determined from the product of the flexural rigidity and the curvature), the differential equation of the deflection curve is

$$EI\frac{d\theta}{ds} = -Pz \tag{3.8}$$

for the applied load P on a beam lying along the y-axis. After manipulating this equation with the geometrical relations given in the book by S.P. Timoshenko [15], results for the deflections and rotations are tabulated numerically using elliptic integrals. The following results can be found as functions of p, which is directly related to the rotation θ:

$$\begin{aligned}
\text{applied load, } P &= \frac{K(p)^2 EI}{L^2} && (3.9)\\
\text{y-displacement, v} &= 2\left[E(p)\sqrt{\frac{EI}{P}} - L\right] && (3.10)\\
\text{z-displacement, w} &= 2p\sqrt{\frac{EI}{P}} && (3.11)\\
\text{x-rotation, } \theta &= 2\sin^{-1} p && (3.12)
\end{aligned}$$

where *K(p)* and *E(p)* are the complete elliptic integrals of the first and second kind, respectively. These integrals can be found as follows:

$$\begin{aligned}
K(p) &= \int_0^{\pi/2} \frac{d\phi}{\sqrt{1 - p^2\sin^2\phi}} && (3.13)\\
E(p) &= \int_0^{\pi/2} \sqrt{1 - p^2\sin^2\phi}\, d\phi && (3.14)
\end{aligned}$$

Beam Element Type	$\frac{v}{L}$ y-displacements		$\frac{w}{L}$ z-displacements		$\frac{\theta}{2\pi}$ x-rotations	
	Value	Difference	Value	Difference	Value	Difference
Analytical	0.3454	8.57%	0.6626	2.62%	0.1944	3.77%
Hermitian beam	0.3451	8.64%	0.6615	2.79%	0.1942	3.88%
2-node isobeam	0.3799	0.56%	0.6833	0.42%	0.2032	0.56%
3-node isobeam	0.3777	<0.01%	0.6804	<0.01%	0.2021	<0.01%
4-node isobeam	0.3777		0.6804		0.2021	

Table 3.2: Case II: convergence properties at the tip for a thick 10-element beam; L = 10

where p is given using Equation 3.12. The loading parameters given in Figure 3-6 result in a rotation up to approximately 70 degrees.

Like the analytical solution in the previous case, these equations are also limited to small strains and do not account for shear deformations. Both of these assumptions introduce errors in the results since shear deformations can only be neglected when the resultant internal reaction is a pure couple and small strains are usually limited to slender beams. For beams with the given set of geometry and loading, the axial load and transverse perturbation load both contribute to additional forces that render the Bernoulli beam assumption inadequate for this case. The magnitude of this error will be evaluated in the following section.

3.2.2 Finite Element Analysis

Figure 3-8 graphically compares the analyses using Hermitian and isobeam elements with the analytical results for the calculation of the normalized nodal y-displacements $\frac{v}{L}$, the normalized nodal z-displacements $\frac{w}{L}$ and the normalized nodal rotations $\frac{\theta}{2\pi}$ at the tip of the beam as the loading increases. Table 3.2 compares the values for the displacements at the tip of the beam of length L = 10, assuming that the four-node isobeam is the most accurate solution.

Similar to the results of the previous case, the results of the analytical solution and the Hermitian beam solution are identical to within 0.1%. Also, the displacements

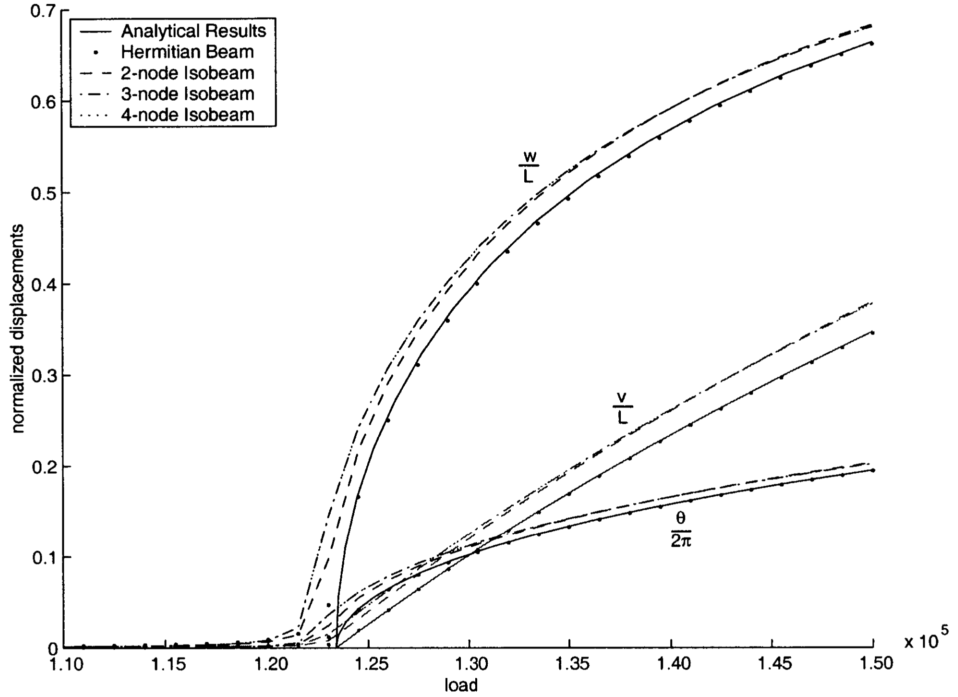

Figure 3-8: Case II: load-displacement plot of tip for a thick beam; L = 10
Note: The results for the three-node and four-node isobeam element are overlapping.

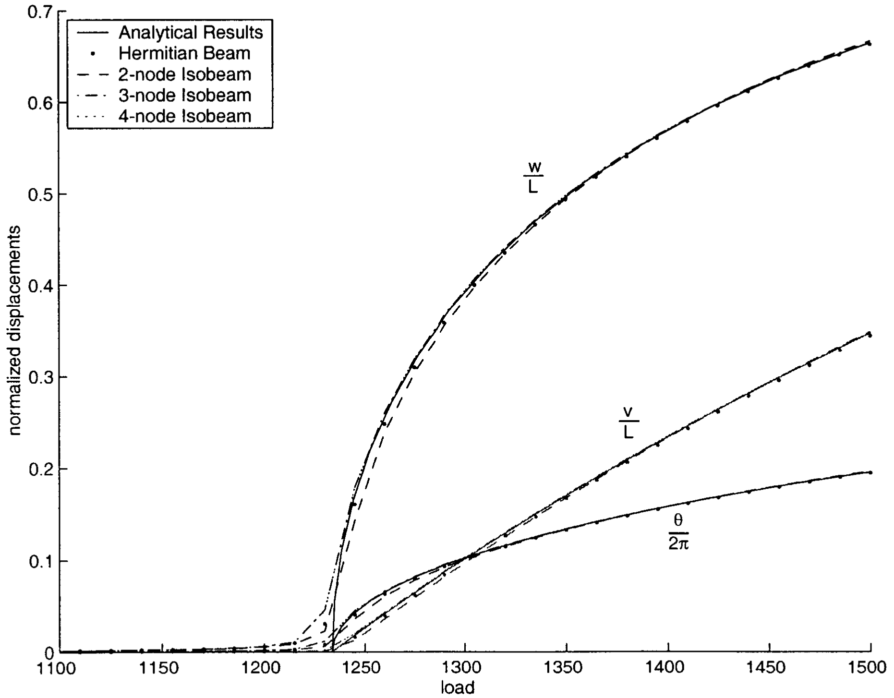

Figure 3-9: Case II: load-displacement plot of tip for a slender beam; L = 100

for the isobeam elements are greater than those for the Hermitian elements and the analytical case, but for this case, the error is larger. When comparing the Hermitian axial displacements with those of the four-node isobeam, the difference rises to 8.6%. There are two reasons for this error. First, like the previous case, there is an error due to the fact that the Bernoulli beam assumption is valid for small strains. Therefore, there are smaller values for displacements using the Hermitian beam element and the analytical solution. Second, the isobeam elements include shear deformations. In this example, the resultant normal and shear forces are nonzero which means that the Bernoulli beam assumption for negligible shear forces is not applicable to this case. Instead, the Timoshenko beam description is a more valid model.

The isobeam elements are equally effective when using the three- and four-node elements. There is a very slight difference when using the two-node element which gives smaller displacements yet is still more accurate than the Hermitian beam element. The results from the two-node isobeam lie below the three- and four-node isobeam and above the Hermitian beam element.

Figure 3-9 shows the same plot for the same beam elongated to length L = 100. As in the previous example, after extending the length of the beam, the results for the isobeam elements converge towards the results for the analyses which neglect shear deformations and assume small strains. For thicker beams, the shear stresses are relatively significant compared to the axial stresses due to bending, and the errors in the analysis increase.

3.2.3 Linearized Buckling Analysis

Another interesting aspect of this problem is the transition to instability due to the compressive forces acting along the beam. The load-displacement plot of Figure 3-8 is characteristic of a loaded beam structure which progresses from stable to unstable equilibrium. The prebuckling displacements, corresponding to $P < P_{cr}$ are relatively small and comparatively linear with respect to the applied loading. The structure is in stable equilibrium. At the instance when the first critical buckling load is reached, the structure buckles and transitions from stable to unstable equilibrium. This transition drastically alters the load-displacement path, and the structure does not function the same as before. Whereas the stable prebuckling behavior was characterized by small displacements per load increment, the unstable postbuckling behavior is characterized by the same-sized load increments producing much larger displacements.

The fastest method for calculating an estimate for the critical buckling loads for this case is by using Euler's column formula:

$$P_e = \frac{\pi^2 EI}{4L^2} \tag{3.15}$$

This equation is derived from the differential equation of the deflection curve which neglects shear deformations and assumes that the beam is initially straight and undergoes small strains. To account for the shear deformations, the differential equation for the deflection curve should account for the additional curvature due to shear. The following correction factor for this beam problem should be used instead [15]:

$$P_{cr} = \frac{P_e}{1 + nP_e/AG} \tag{3.16}$$

where P_e is the Euler buckling load given in Equation 3.15, G is the shear modulus, A is the cross-sectional area of the beam and n is a correctional factor which depends on the cross-sectional geometry ($n = 1.2$ for rectangular beams). Using this correctional factor to include shear effects on the buckling load when Poisson's ratio, $\nu = 0$, the critical load decreases by a factor of about 0.0005 for beams of length L = 10 and 0.005 for beams of length L = 100, a relatively insignificant amount. Table 3.3 shows that for the shorter beam, the correction to include shear effects decreases the error from 0.62% to 0.12%. The relative insignificance of this result agrees with S.P. Timoshenko's conclusion [15] for solid columns. Timoshenko has found that the ratio $1/(1 + nP_e/AG)$ is almost always close to unity for solid beam elements since $nP_e \ll AG$.

As described in Section 2.5, there are two methods with which the critical buckling loads can be determined using the finite element method: classical and secant. Tables 3.3, 3.4 and 3.5 compare the calculated values for the buckling loads using

Beam Element Type	Classical Method Buckling Load	Difference	Secant Method Buckling Load	Difference
Hermitian beam	123114	0.41%	123111	0.41%
2-node isobeam	123115	0.41%	122986	0.35%
3-node isobeam	122612	< 0.01%	122485	0.10%
4-node isobeam	122612		122485	0.10%
Analytical - no shear	123370	0.62%		
Analytical - shear	122764	0.12%		

Table 3.3: Case II: calculation of the smallest critical buckling load for a thick beam using a small perturbation load; L = 10 and $\beta = 2 \times 10^{-4}$

Beam Element Type	Classical Method Buckling Load	Difference	Secant Method Buckling Load	Difference
Hermitian beam	1233.68	< 0.01%	1230.82	0.23%
2-node isobeam	1238.72	0.41%	1235.82	0.18%
3-node isobeam	1233.63	< 0.01%	1230.74	0.23%
4-node isobeam	1233.62		1230.74	0.23%
Analytical - no shear	1233.70	0.01%		
Analytical - shear	1233.64	< 0.01%		

Table 3.4: Case II: calculation of the smallest critical buckling load for a slender beam using a small perturbation load; L = 100 and $\beta = 2 \times 10^{-4}$

Beam Element Type	Classical Method Buckling Load	Difference	Secant Method Buckling Load	Difference
Hermitian beam	1233.68	< 0.01%	1169.19	5.22%
2-node isobeam	1238.72	0.41%	1173.80	4.85%
3-node isobeam	1233.63	< 0.01%	1168.89	5.25%
4-node isobeam	1233.62	< 0.01%	1168.89	5.25%
Analytical - no shear	1233.70	0.01%		
Analytical - shear	1233.64	< 0.01%		

Table 3.5: Case II: calculation of the smallest critical buckling load for a slender beam using a large perturbation load; L = 100 and $\beta = 10^{-3}$

these two methods. Each of these three tables corresponds to varying values of the length of the beam and the size of the perturbation load. Table 3.3 is the same case that was analyzed for the load-displacement plot of Figure 3-8, and likewise, Table 3.4 matches the elongated beam of Figure 3-9. In addition, a third variant used for Table 3.5 matches that of Table 3.4 except that the perturbation load has been increased from $\beta = 2 \times 10^{-4}$ to $\beta = 10^{-3}$. All of the results were compared to the four-node isobeam element for the particular beam length and $\beta = 10^{-3}$, since it includes shear effects, accounts for large strains and includes minimal effects due to the perturbation load.

The findings support the various ways in which errors due to neglecting shear deformations and assuming small strains can be minimized as discussed for the previous case. As discussed above, when shear effects are included in the analytical buckling calculations, the error decreases to 0.12%. This remaining error is due to the assumption of small strains. Analytical solutions are rare though and only exist for few problems. When performing a finite element analysis, one way to minimize errors is the choice of beam element. Although the buckling results from the Hermitian beam and the isobeam models differ by less than 1% in each case, this error results from the assumption of negligible shear deformations and small strains in the Hermitian beam elements. When using slender beams, the error for most of the element models using the classical method are decreased to much less than unity. This effectively disregards the need to include terms to account for shear and large strains since those factors are minimal. As described in the previous case, the discrepancy results partially from shear deformation assumptions, but also from the assumption of small strains in the analytical and Hermitian beam results.

The Euler column buckling load and the classical method of the linearized buckling analysis provide essentially the same results since they take advantage of the same assumptions. In general, the buckling loads calculated using the secant method are less than those calculated using the classical method or analytically. The errors are magnified from less than 1% to approximately 5% when the perturbation load increases from $\beta = 2 \times 10^{-4}$ to $\beta = 10^{-3}$. Although this reflects up to a 5% inaccuracy in comparison to the analytical and classical result, the results are relatively constant. The key assumption governing the secant formulation is not as strong as the key assumption governing the classical formulation. Namely, the prebuckling total stiffness matrix is more easily broken down into a constant, loading-independent linear part and a linearly-varying, loading-dependent nonlinear part as developed in the classical theory. This is a stronger assumption than by assuming, as in the secant formulation, that the total stiffness matrix varies linearly from the previous timestep to the next. The formulations yield of course different results, and in this example the classical formulation for the linearized buckling load is more accurate.

Table 3.5 reflects how the perturbation load can skew the accuracy of the analysis. The perturbation load is necessary to introduce an initial imperfection into the problem which would, in turn, induce unstable equilibrium. This load should be small so that the results do not directly depend on its magnitude. One way to examine the effects of the perturbation is to view the load-displacement history, and determine if the displacements that are directly resulting from the perturbation load are excessively large. If so, then the perturbation load may be affecting the results. Figure 3-10 compares the effect of different values of the perturbation load on the displacement history. Just before reaching the critical load, the z-displacements are much larger when $\beta = 10^{-2}$ than when it increases to $\beta = 2 \times 10^{-4}$. The same beam which is loaded by the larger perturbation load develops errors as large as 5.25% using the secant method for the linearized buckling analysis. Therefore, the secant method is accurate as long as the perturbation load does not affect the bending behavior significantly.

As shown in Table 3.5, when the perturbation load increases, the secant method approximation to the critical load decreases. When the perturbation load is small, the secant method is just as accurate as the classical method. Although there are errors, the method is still reliable as a more conservative estimate of the critical buckling load. To determine why the secant method estimates the buckling load conservatively, one should compare the governing assumptions underlying the secant and classical formulations of the linearized buckling analysis as discussed in Section 2.5. The

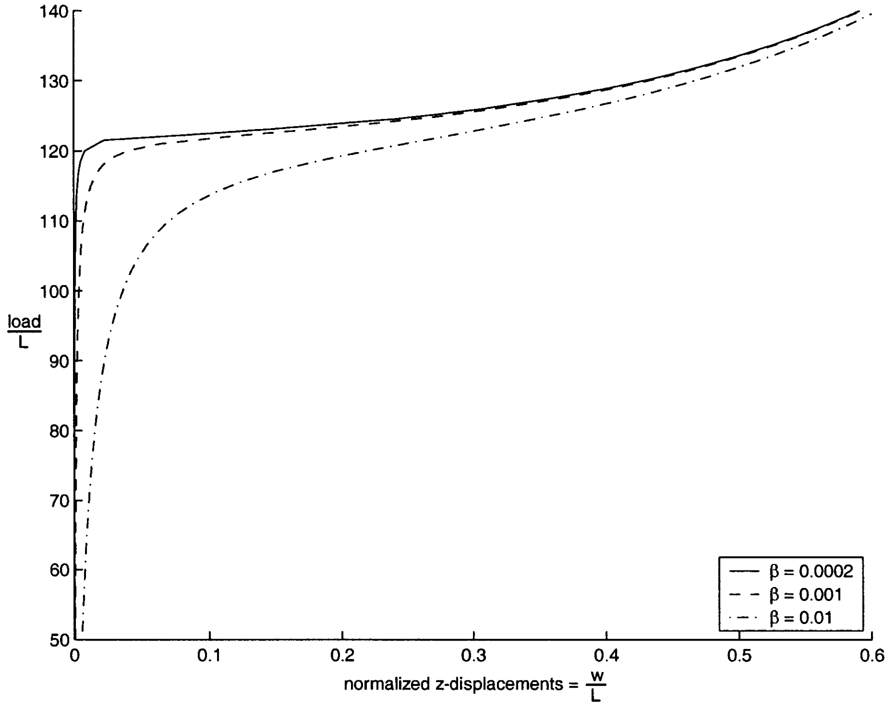

Figure 3-10: Case II: comparison of z-displacement response of the tip for a thick beam under various perturbation loads; L = 10

secant method assumes that in prebuckling the elements of the stiffness matrix vary linearly from one timestep to the next. When the perturbation load is relatively large, this assumption starts to become invalid. Figure 3-10 shows how the bending behavior alters as the perturbation load increases. The prebuckling z-displacement ($\frac{w}{L}$) displacements become increasingly nonlinear as β increases. This is surprising considering the secant method takes into account the nonlinear aspect of the stiffness matrix, whereas the classical method assumes it varies linearly with respect to time. Therefore, mathematically the secant method should be more reliable. Further study into this problem is needed to completely understand this phenomenon.

When using the secant method for the linearized buckling analysis, it is useful to see how the estimated buckling loads vary as the perturbation load varies since it is not sufficient to assume that the solution is accurate if $\beta \ll 1$.

3.3 Right-Angle Frame Under End Load

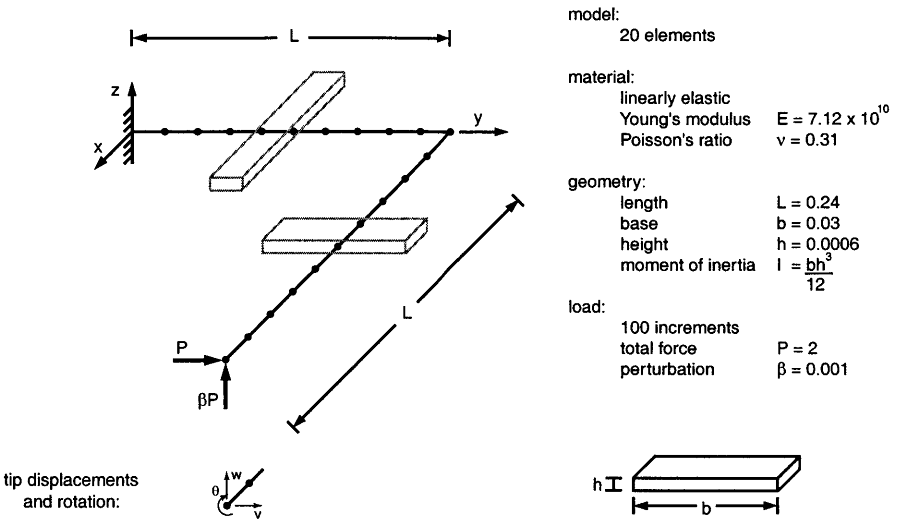

Figure 3-11: Right-angle frame under end load: finite element model

This example is an assemblage of two beams connected in the manner of a right-angle frame shown in Figure 3-11. The cross-section is extremely thin as shown in the figure. The structure is modelled using 20 beam elements (10 per section) which are initially straight and of constant rectangular cross section. A force P and a relatively small perturbation load βP acts at the tip of the structure, and the resulting three-dimensional motion is shown in Figure 3-12. The three configurations correspond to the initial undeformed configuration P = 0, an intermediate load which is slightly larger than the first buckling load P = 1.2 and the much larger final load P = 2.0. The deformed configurations show that the motion is more complicated than either of the two previous examples, but the discussions in Sections 3.1 and 3.2 are useful when interpreting and understanding the various mechanisms that apply to the present case.

One interesting aspect of this case is that buckling is not caused directly from compression due to the applied load as for the previous case for the beam under compressive axial load. This results from the fact that the structure is extremely thin as can be seen by the specifications provided in Figure 3-11. The aspect ratio of

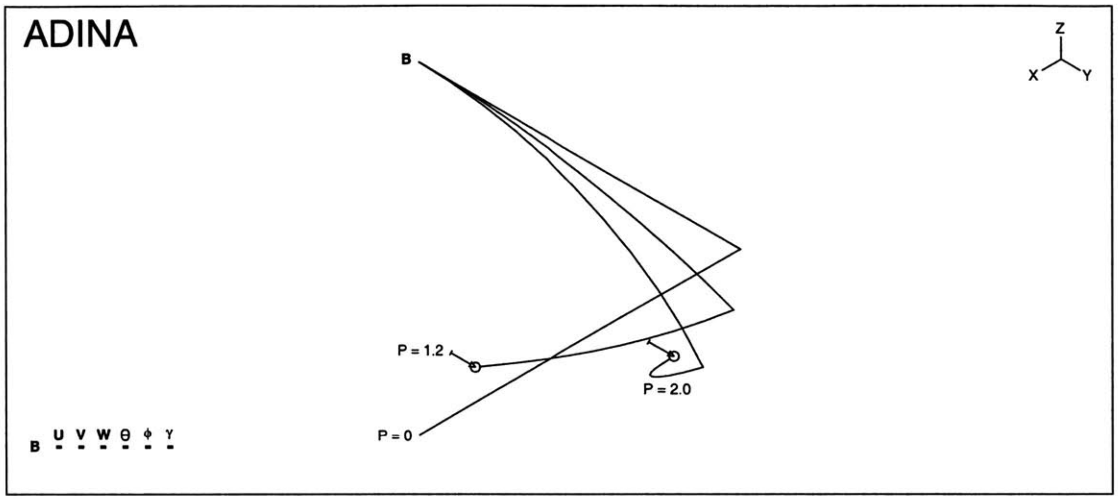

Figure 3-12: Case III: motion following load application: ADINA results

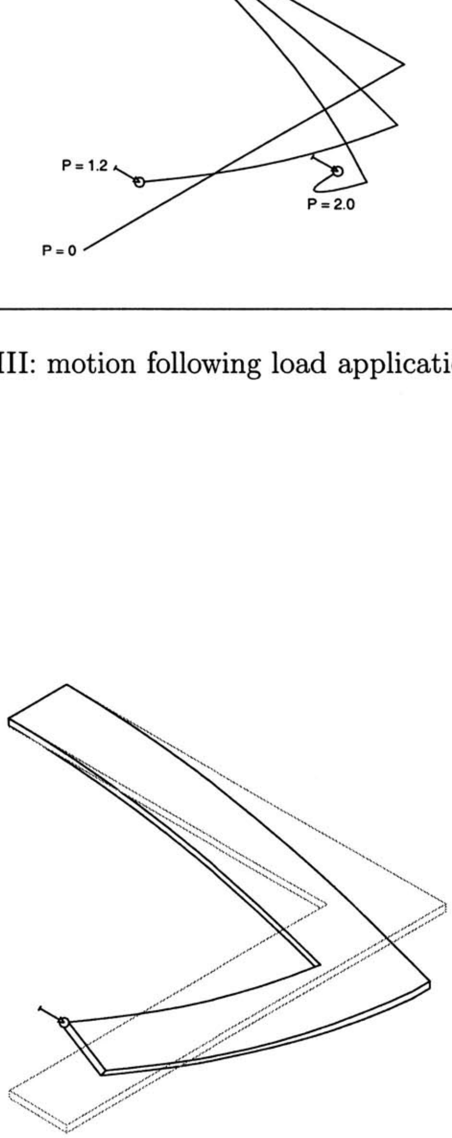

Figure 3-13: Case III: twisting motion following load application

width-to-height is 50:1, and the load acts parallel to the width of the structure. In addition, Figure 3-13 shows the frame with exaggerated thickness under the loading. As the load P increases with time, the outer arm (from the right-angle joint to the free tip) begins to twist with respect to the x-axis whereas the inner arm (from the fixed end to the right-angle joint) follows. The resulting motion leaves the right-angle frame with compression acting along the outer edges as shown in Figure 3-13, and tension along the inner edges. The compression along the outer edges causes buckling.

This problem has been studied by J.H. Argyris *et.al.* [2] to calculate the buckling load using a different finite element modelling technique. There are also other texts which predict the deformation of this right-angle frame using linear displacement assumptions for small displacements and loads much smaller than the critical buckling load, $\mathrm{P} \ll \mathrm{P}_{cr}$.

3.3.1 Finite Element Analysis

The results of the finite element analysis are shown in Figure 3-14 for the normalized displacements along the y-axis ($\frac{v}{L}$), the normalized displacements along the z-axis ($\frac{w}{L}$) and the normalized rotations around the x-axis ($\frac{\theta}{2\pi}$) where v and w are the tip displacements and θ is the x-rotation at the tip. The plot shows that the rotation term $\frac{\theta}{2\pi}$ is greater than either of the other displacement terms. This is different than in the previous two cases where the transverse displacement term dominated. In this case, the large rotation term at the tip of the right-angle frame corresponds to a twisting moment on the leg of the frame on which the load is applied. This problem clearly includes warping torsion in addition to bending displacements.

Table 3.6 compares the convergence properties of the finite element analysis when examining the displacements at the tip of the structure. Assuming that the four-node isobeam element is the most accurate, the error analysis uses this model to compute the accuracy. As in the previous examples, the values of the displacements at the tip using the isobeam element converge as the number of nodes increases, yet the two-node isobeam element still gives accurate results to within 0.29%.

Also, the results show that the Hermitian beam yields approximately the same

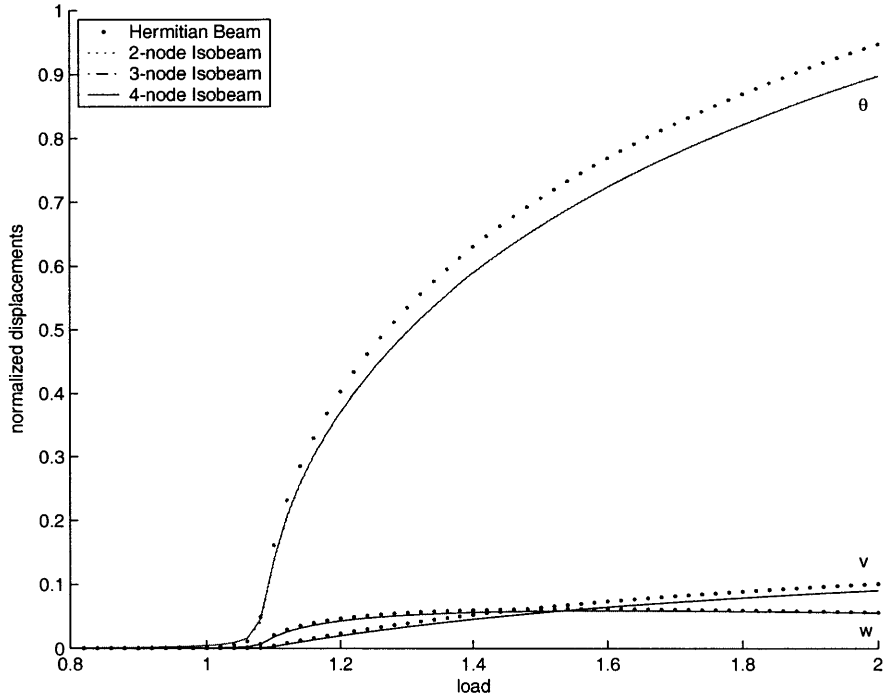

Figure 3-14: Case III: load-displacement plot of tip of the right-angle frame.
Note: The results for the two-, three- and four-node isobeam elements are overlapping.

Beam Element Type	$\frac{v}{L}$ y-displacements		$\frac{w}{L}$ z-displacements		$\frac{\theta}{2\pi}$ rotations about the negative x-axis	
	Value	Difference	Value	Difference	Value	Difference
Hermitian beam	0.1009	11.59%	0.0563	1.33%	0.9477	5.59%
2-node isobeam	0.0906	0.21%	0.0554	0.29%	0.8985	0.11%
3-node isobeam	0.0904	$<$0.01%	0.0555	$<$0.01%	0.8975	$<$0.01%
4-node isobeam	0.0904		0.0555		0.8975	

Table 3.6: Case III: isobeam convergence properties at the tip

error as found in the previous example for which the error remained below 9% in the displacements. In this case, the largest error rises to about 11.6%. The similarity in error analysis indicates that the errors using the Hermitian beam element most likely stem from the same source: the presence of shear deformations and large strains.

3.3.2 Linearized Buckling Analysis

Buckling of this beam structure occurs due to a combination of bending and torsion. S.P. Timoshenko studied a similar example in Reference [15] for a right-angle structure with one end fixed and the other simply-supported. For that case, two solutions for the critical buckling load were found corresponding to flexural buckling and purely torsional buckling by solving the governing differential equations for bending and torsion. The solution to the governing equations for this problem exists when the load is smaller than the flexural Euler load for buckling. The results of this analysis are 1.648 for the critical flexural buckling load and 1.018 for the critical purely torsional buckling load. The latter solution governs the buckling behavior of the frame since it is smaller. This solution is comparable to the results using the classical method in Table 3.7 for a fixed-free frame and differs from the four-node element by approximately 6%. Since the structure is more likely to buckle due to torsion, it is important to correctly model the beam structure using the appropriate warping displacement functions as described in Section 2.6.

Tables 3.7 and 3.8 compare the results of various buckling analyses. The latter uses a perturbation load factor $\beta = 10^{-5}$. From Figure 3-14, we can see that the Hermitian beam and isobeam incremental large displacement analyses using the LDC method both predict that the initial buckling load lies within the load interval bounded approximately by $1.0 < \mathrm{P} < 1.2$. The analytical result for the simply-supported frame also pinpoints the critical buckling load at slightly above 1.01. Therefore, we can assume that larger errors arise when using the Hermitian beam elements or the secant method since those results are no larger than 0.87 and are much smaller than those predicted by the load-displacement plots and the analytical analysis. Although there are no definitive solutions for this case, we can infer from analytical methods of similar

Beam Element Type	Classical Method Buckling Load	Difference	Secant Method Buckling Load	Difference
Hermitian beam	0.5475	49.62%	0.2835	73.92%
2-node isobeam	1.0883	0.12%	0.4096	62.31%
3-node isobeam	1.0868	0.17%	0.4090	62.37%
4-node isobeam	1.0869	< 0.01%	0.4090	62.37%

Table 3.7: Case III: calculation of the smallest critical buckling load using a large perturbation load; $\beta = 10^{-3}$

Beam Element Type	Classical Method Buckling Load	Difference	Secant Method Buckling Load	Difference
Hermitian beam	0.5473	49.65%	0.5473	49.65%
2-node isobeam	1.0885	0.14%	0.8716	19.81%
3-node isobeam	1.0877	0.06%	0.8708	19.89%
4-node isobeam	1.0870		0.8707	19.89%

Table 3.8: Case III: calculation of the smallest critical buckling load using a small perturbation load; $\beta = 10^{-5}$

cases and from the general numerical results using the more general isobeam element an approximate value for the buckling load. The error analyses of Tables 3.7 and 3.8 are performed with respect to the buckling load calculated using the four-node isobeam element under the classical method with $\beta = 10^{-5}$.

The results remain relatively constant when varying the number of nodes of the isobeam elements. This reflects the same pattern as in the previous cases. The two-node element gives results for the displacement field and the linearized buckling load that are accurate to within 1% of the four-node isobeam element.

Another notable characteristic of Table 3.7 is that the error increases to 50% using the Hermitian beam element. In case II, the error was negligible between the two element models when calculating the buckling load. This case differs by the existence of warping torsion, but the Hermitian beam elements and the isobeam elements both include warping torsion displacements using displacement interpolation functions given in Reference [5]. Torsion is not the cause of the errors that stem from using the Hermitian beam elements rather than the isobeam elements. Instead, this discrepancy arises due to the limitations of the linear variation in axial displacements adopted by the axial displacement function for the Hermitian beam elements. The linear approximation is not sufficient to model more complex axial displacement variations in the beam structure. Conversely, the isobeam element is based on a mixed interpolation of displacements and stresses that is capable of accurately modelling the beam structure. It is surprising that this difference is so large for the displacements as a function of the load history. Figure 3-14 shows that the response is not much different between the isobeam and Hermitian beam element for the buckling load. Calculating the buckling load with the Hermitian beam incrementally using the LDC method (see Section 2.5) yields much more accurate results than using the linearized buckling method with that particular beam element. The isobeam element yields accurate results using either solution technique: the classical linearized buckling method or the incremental LDC method.

Similar to the results for the linearized buckling analysis for the second example, there is a significant discrepancy between the secant and classical formulations with each returning consistent results. However, unlike in the previous example, the secant method analysis provides a significantly more conservative estimate. The classical method holds up quite well in this case since it assumes that the nonlinear part of the stiffness matrix is linear for small precollapse timesteps whereas the linear part remains constant.

Of course, the classical buckling solution is close to the analytical solution since the same assumptions are used, but in this case we find a large discrepancy between those results and that using the secant buckling method. One may expect better results from the secant method rather than the classical method, but that is not reflected in this case. The secant method takes into account the total stiffness matrix and maintains its nonlinearity, whereas the classical method assumes that the stiffness matrix can be divided into a constant stiffness matrix K_L that is independent of the loading and a varying nonlinear stiffness matrix K_{NL} that is dependent on the loading. Since the secant method is more general, one would expect that this formulation would yield more accurate results. Further research and numerical experimentation is necessary in order to see the cause of this behavior.

The combination of torsion and flexure effects on the calculation of the buckling load retains the discrepancies that were discovered in the two previous examples. There are some surprising results where we find that the classical method is more general for nonlinear displacements than the secant method for linearized buckling analysis and also, the Hermitian beam element yields surprisingly inaccurate results for the buckling load using the linearized buckling analysis but works quite well using the incremental LDC method. Further research must be done, and a shell analysis would be an appropriate way to proceed in order to ascertain the cause of these discrepancies.

Chapter 4

Conclusions

The examples described in the previous chapter examine the effect of various theoretical assumptions which are commonly used to model one-dimensional, slender structures and their displacement and buckling behavior. Depending on the geometry and applied loading, various assumptions can be applied in order to decrease the time needed to complete the finite element analysis.

The choice between Hermitian beam elements and isobeam elements depends on the magnitude of the strains and shear forces acting on the structure. The simplest analysis using two-node Hermitian beams is reliable for structures undergoing negligible shear forces and small strains since the analysis neglects shear effects using the Bernoulli beam assumption and neglects higher-order strain terms. For most large displacement analyses of slender beam structures, either element can be used. However, when performing an analysis in the presence of moderate strains and/or shear forces, Hermitian beam elements may be unreliable.

The errors that develop when varying the number of nodes of the isobeam element are negligible as long as a reasonable number of elements is used. The errors between the two-node element compared to the four-node element never rose over 2% when evaluating the load-displacement history or the buckling load.

For the linearized buckling analysis, the secant formulation is a more conservative estimate for the calculation of the critical buckling load in the cases examined in this thesis. When applying the secant formulation, one must be sure to see if the perturbation load factor β is small enough. It is not sufficient to assume the analysis is accurate if $\beta \ll 1$. For beam structures under complex loading, larger errors may arise using the Hermitian beam element due to the limitations of the linear variation in the axial displacement interpolation function. Otherwise, the results are consistent and reliable for simply loaded structures. On the other hand, the classical formulation is very accurate and reliable for all of the given examples.

By examining these modelling techniques, we establish rules by which one can apply the finite element method for more complicated slender, one-dimensional structures. A thorough understanding of the theory behind the finite element method provides a means to most effectively interpret the results of the analysis.

Appendix A

Cantilever Beam Subjected to Transverse Load

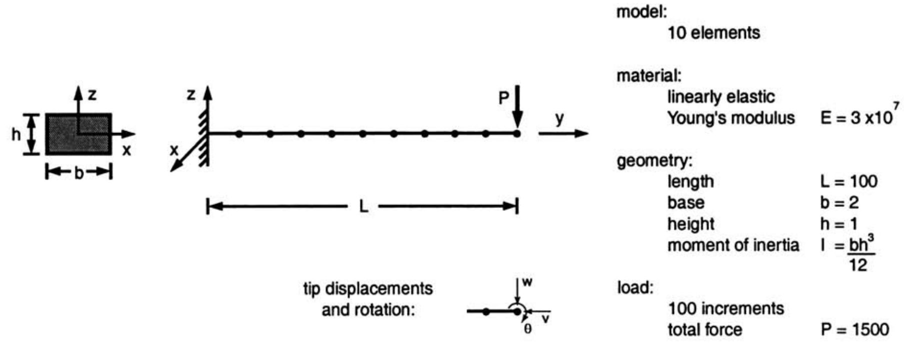

Figure A-1: Cantilever beam under transverse load: finite element model

The problem of a linear elastic cantilever beam subjected to a transverse load is represented by the finite element model shown in Figure A-1 using ten beam elements. The motion following the load application is shown in Figure A-2 for the initial undeformed beam and the deformed beam under the total applied load.

Figure A-3 compares the load-displacement results from the finite element analysis with analytical results derived using elliptic integrals in Reference [11] by K. Mattiasson. The results differ from the ADINA analysis using Hermitian beam elements by less than 1%.

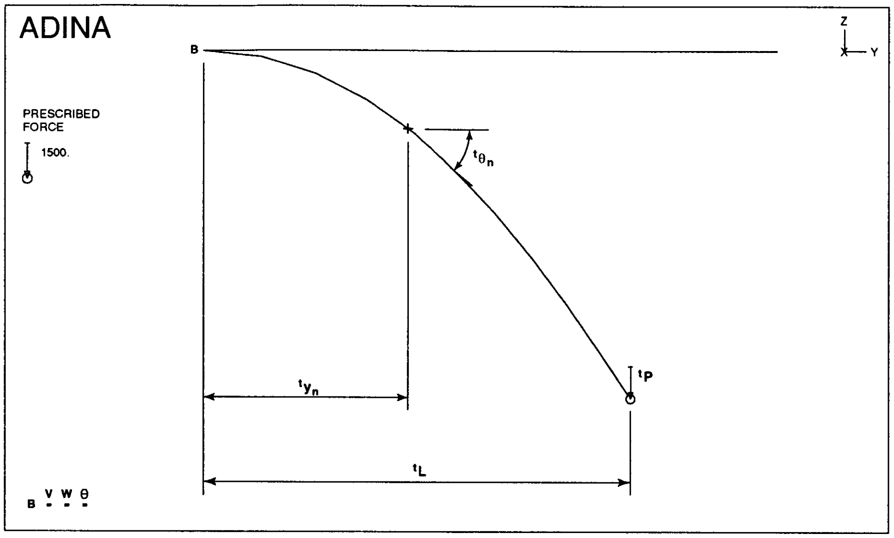

Figure A-2: Case IV: motion following the load application

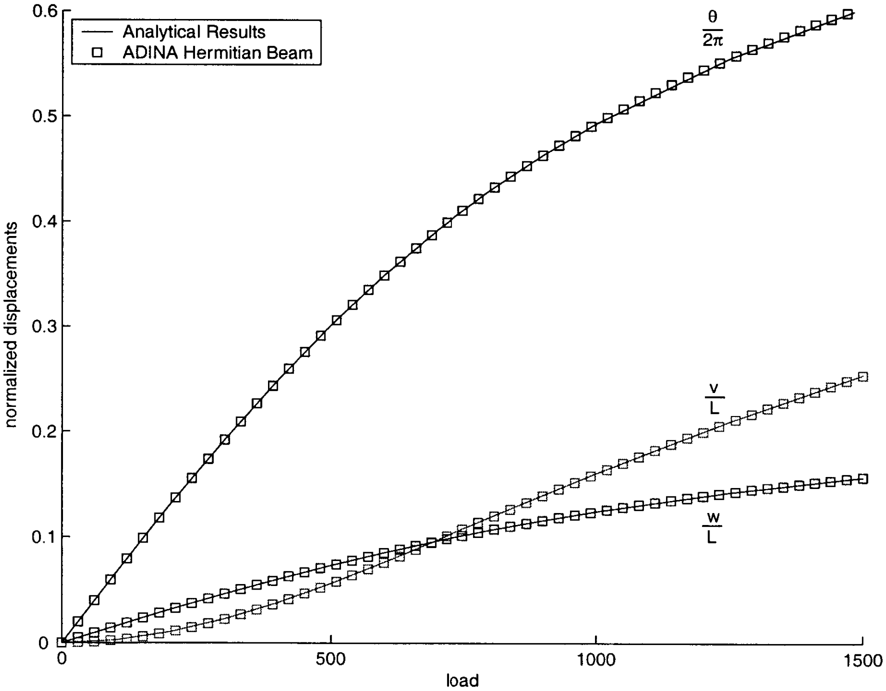

Figure A-3: Case IV: load-displacement plot of the tip

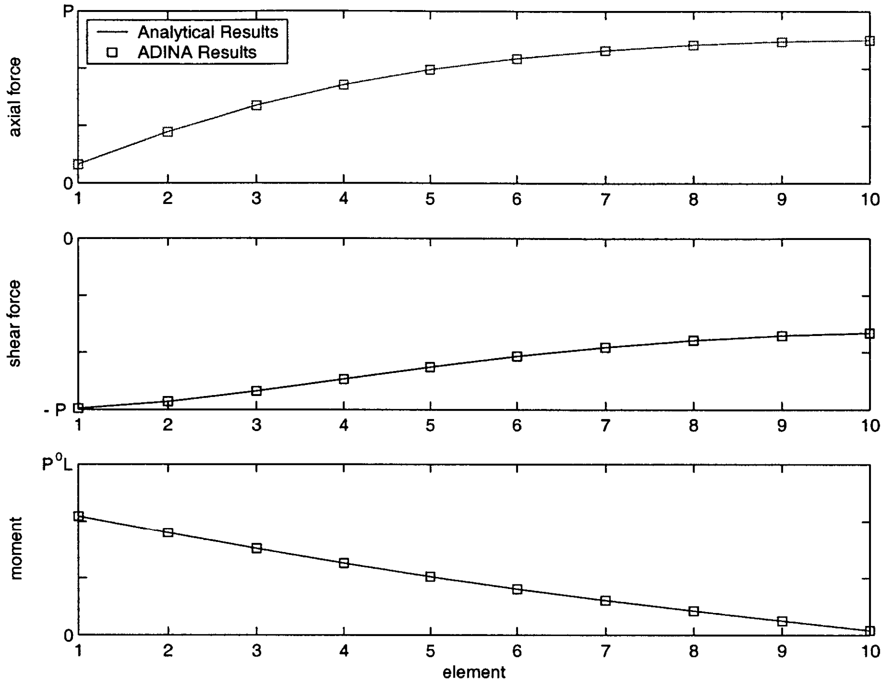

Figure A-4: Case IV: axial forces, shear forces and moments along the beam with load P = 1500 modelled using 10 elements

Figure A-4 compares the analytical and finite element analysis results for the axial force, shear force and moment over each element along the beam at the final timestep corresponding to P = 1500. The analytical results were obtained for the large displacement case assuming that the applied loading, which can be separated into axial and transverse components, induces an equal and opposite reactive force along the beam. Using the nodal rotations calculated analytically in Reference [11] for an incremental large displacement analysis, the axial forces, shear forces and moments are determined using simple geometric relations. Given the x-rotation ${}^t\theta_n$ of beam element n at time t, the forces and moments are given by the following relations:

$$\text{axial force, } {}^tR_n = {}^tP \sin({}^t\theta_n) \tag{A.1}$$

$$\text{shear force, } {}^tV_n = {}^tP \cos({}^t\theta_n) \tag{A.2}$$

$$\text{moment, } {}^tM_n = {}^tP\,({}^tL - {}^ty_n) \tag{A.3}$$

where ${}^{t}P$ is the applied loading at the tip at time t, ${}^{t}y_n$ is the position of the node along the y-axis with respect to the fixed node at time t and ${}^{t}L$ is the total length of the beam along the y-axis at time t as illustrated in Figure A-2. As exhibited in Figure A-4, the finite element analysis gives an accurate estimate of the axial forces, shear forces and moments along the beam.

When using a coarser mesh, a noticeable discrepancy develops between the finite element ADINA results and the analytical results when calculating the axial forces, shear forces and moments along the beam. Figure A-5 compares the response when the number of elements for the finite element model decreases to three. This follows from the fact that the stress-strain law and compatilibity between the elements is satisfied exactly whereas the stress equilibrium is satisfied approximately.

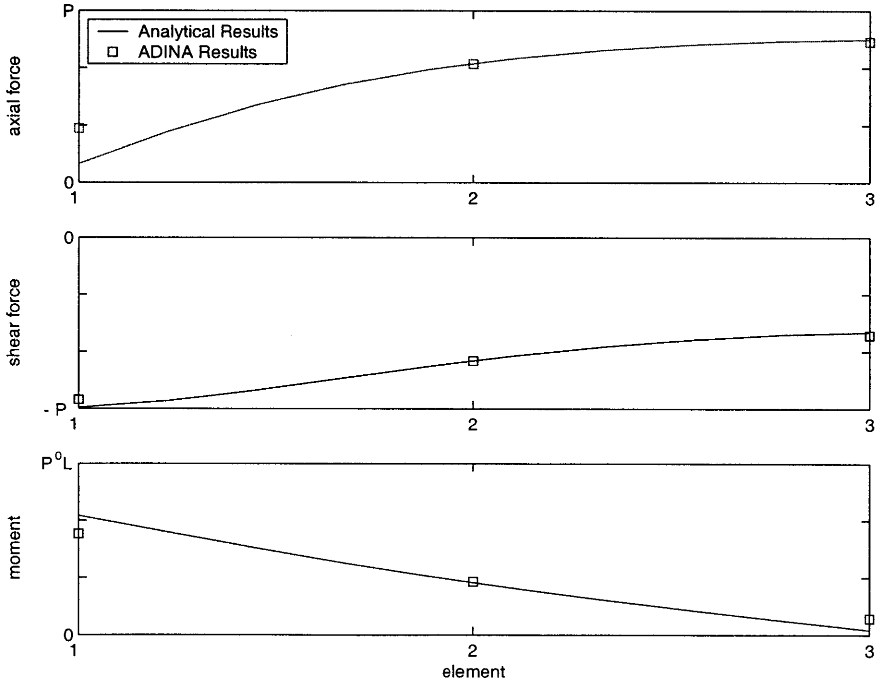

Figure A-5: Case IV: axial forces, shear forces and moments along the beam with load P = 1500 modelled using 3 elements

Appendix B

Implementation of the Nonlinear Finite Element Beam Equations

The objective of this work is to gain more insight into the evaluation of geometrically nonlinear beam structures. Through the evaluation of various case studies, the results were analyzed and compared in order to determine advantages to using different modelling techniques. To further understand the nonlinear finite element analysis of beam structures, the equations and procedures described above have been directly applied to these studies. The nonlinear finite element analysis using Hermitian beam elements described in Chapter 2 has been implemented using MATLAB. This implementation was performed in order to better understand the application of the finite element equations and the general sequence of algorithms used to perform an analysis.

The equations were implemented into a source code named CR, using the method described in Reference [4] for Hermitian beam elements. All integrations were performed over rectangular cross-sections using Mathematica and imported as subfunctions of CR which is completely evaluated using MATLAB. The linear and nonlinear strain-displacement transformation matrices were constructed using the beam interpolation functions given in the Reference [4]. The complete analysis assembles the linear and nonlinear stiffness matrices and nodal point force vector at each incremental load step and performs Newton-Raphson iterations to satisfy equilibrium at sufficient convergence.

The code was then tested using Case IV and Case I. Figure B-1 compares the results for Case IV, a beam subjected to a transverse force at the tip with specifications given in Figure A-1, and Figure B-2 compares the results for Case I, a beam subjected to an end moment at the tip with specifications given with Figure 3-1. Both cases show that the results are accurate, but slight errors arise as the load increases. This results from convergence errors rather than flaws in the theory. Further optimization of the code is necessary before performing more complex analyses. These examples allowed me to more thoroughly understand the theory described in Chapter 2 and how the theory can be directly applied to beam structures.

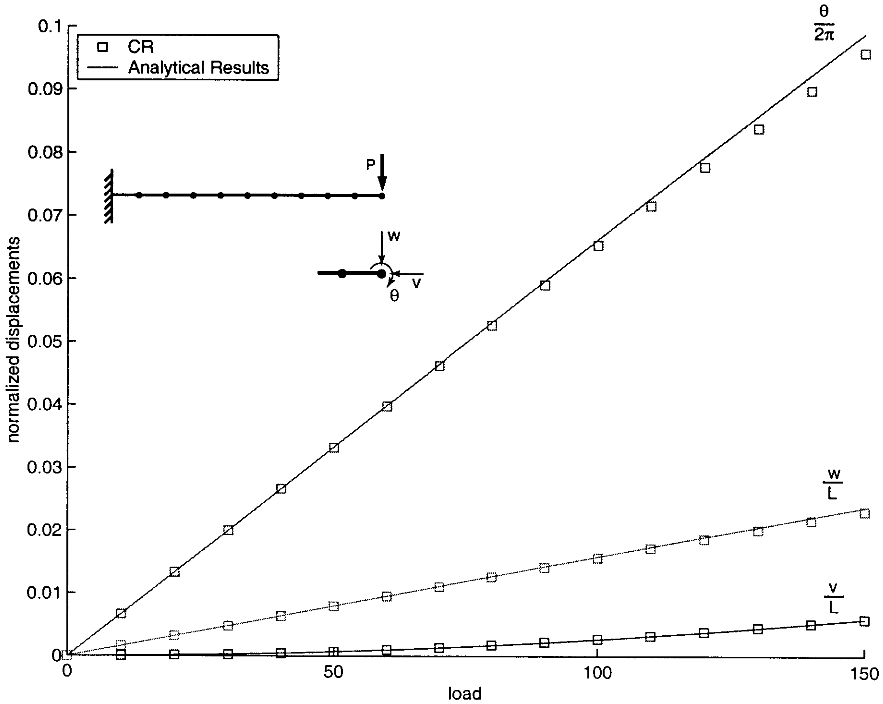

Figure B-1: Case IV: Implementation results

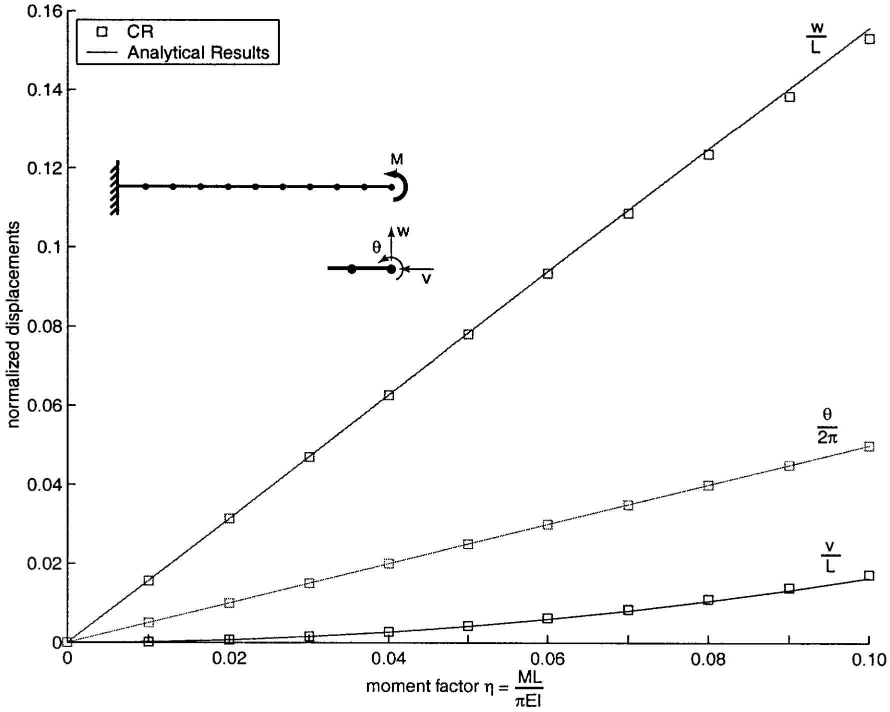

Figure B-2: Case I: Implementation results

Bibliography

[1] ADINA R & D, Inc, Watertown, MA. *Theory and Modeling Guide, Volume 1: ADINA, Report ARD 99-7*, May 1999.

[2] J.H. Argyris, O. Hilpert, G.A. Malejannakis, and D.W. Scharpf. On the geometrical stiffness of a beam in space – a consistent virtual work approach. *Comp. Methods Appl. Mech. Eng*, 20:105–131, 1979.

[3] K.J. Bathe. *Finite Element Procedures.* Prentice Hall, Upper Saddle River, NJ, 1996.

[4] K.J. Bathe and S. Bolourchi. Large displacement analysis of three-dimensional beam structures. *Int. J. Numer. Meth. Engng*, 14:961–986, 1979.

[5] K.J. Bathe and A.B. Chaudhary. On the displacement formulation of torsion of shafts with rectangular cross-sections. *Int. J. Num. Meth. Engng*, 18:1565–1580, 1982.

[6] Z. Bittnar and J. Bittnar. *Numerical Methods in Structural Mechanics.* ASCE Press, New York, 1996.

[7] F. Bleich and L.B. Ramsey. *Buckling Strength of Metal Structures.* Engineering Societies Monographs. McGraw-Hill, New York, 1952.

[8] J.M. Gere and S.P. Timoshenko. *Mechanics of Materials.* PWS, Boston, MA, 4th edition, 1997.

[9] M.B. Kanchi. *Matrix Methods of Structural Analysis.* John Wiley & Sons, New York, 2nd edition, 1993.

[10] C.F. Kollbrunner. *Torsion in Structures: An Engineering Approach.* Springer-Verlag, New York, 1969.

[11] K. Mattiasson. Numerical results from large deflection beam and frame problems analyzed by means of elliptic integrals. *Int. J. Num. Meth. Engng*, 17(1):145–153, 1981.

[12] P.F. Pai and A.L. Palazotto. Large-deformation analysis of flexible beams. *Int. J. Solids Structures*, 33(9):1335–1353, 1996.

[13] E.P. Popov. *Engineering Mechanics of Solids.* Prentice Hall, Englewood Cliffs, NJ, 1990.

[14] J.S. Przemieniecki. *Theory of Matrix Structural Analysis.* McGraw-Hill, New York, 1968.

[15] S.P. Timoshenko. *Theory of Elastic Stability.* McGraw-Hill, New York, NY, 2nd edition, 1961.

[16] S.P. Timoshenko and J.N. Goodier. *Theory of Elasticity.* McGraw-Hill, New York, NY, 2nd edition, 1951.